1 **Floodwater Impact on Galveston Bay Phytoplankton Taxonomy, Pigment Composition and Photo-**
2 **Physiological State following Hurricane Harvey from Field and Ocean Color (Sentinel-3A OLCI)**
3 **Observations**
4
5

7 **Bingqing Liu[1], Eurico J. D'Sa[1*] and Ishan D. Joshi[1]**

9 [1]Department of Oceanography and Coastal Sciences, College of the Coast and Environment, Louisiana
10 State University, Baton Rouge, LA 70803, USA
11 * Corresponding author: ejdsa@lsu.edu

13
14 **Abstract**

15 Phytoplankton taxonomy, pigment composition and photo-physiological state were studied in Galveston
16 Bay (GB), Texas (USA) following the extreme flooding associated with Hurricane Harvey (August 25–29,
17 2017) using field and satellite ocean color observations. Percentage of chlorophyll a (Chl a) in different
18 phytoplankton groups were determined from a semi-analytical IOP (inherent optical property) inversion
19 algorithm. The IOP inversion algorithm revealed the dominance of freshwater species (cyanobacteria and
20 green algae) in the bay following the hurricane passage (September 29, 2017) under low salinity
21 conditions associated with the discharge of floodwaters into GB; 2 months after the hurricane (October
22 29–30, 2017), under more seasonal salinity conditions, the phytoplankton community transitioned to an
23 increase in small sized groups such as haptophyte and prochlorophyte. Sentinel-3A OLCI-derived Chl a
24 obtained using a red/NIR band ratio algorithm for the turbid estuarine waters was highly correlated ($R^2 >$
25 0.90) to HPLC-derived Chl a concentrations. A Non-Negative Least Square (NNLS) inversion model was
26 then applied to OLCI-derived Chl a maps of GB to obtain spatiotemporal distributions of phytoplankton
27 diagnostic pigments; results appeared consistent with extracted phytoplankton taxonomic composition
28 derived from the IOP inversion algorithm. OLCI-derived diagnostic pigment distributions also exhibited
29 good agreement with HPLC measurements, with mean R^2 ranging from 0.39 for violaxanthin to 0.98 for
30 Chl a. Environmental factors (e.g. floodwaters) combined with phytoplankton taxonomy also strongly
31 modulated phytoplankton physiology in the bay as indicated by measurements of photosynthetic
32 parameters with a Fluorescence Induction and Relaxation (FIRe) system. Phytoplankton in well-mixed
33 waters (mid-bay area) exhibited maximum PSII photochemical efficiency (F_V/F_M) and low effective
34 absorption cross section (σ_{PSII}), while the areas adjacent to the shelf (likely nutrient-limited) showed low
35 F_V/F_M and elevated σ_{PSII} values. Overall, the approach using field and ocean color data combined with
36 inversion models allowed, for the first time, an assessment of phytoplankton response to a large
37 hurricane-related floodwater perturbation in a turbid estuarine environment based on its taxonomy,
38 pigment composition and physiological state.

39
40
41
42
43
44
45 **Key words**: Galveston Bay, phytoplankton taxonomy, pigment composition, physiology, ocean color,
46 chlorophyll a, Sentinel-3A OLCI
47
48

1. Introduction

Phytoplankton, which form the basis of the aquatic food web, are crucial to marine ecosystems and play a strong role in marine biogeochemical cycling and climate change. Phytoplankton contributes approximately half of the total primary production on Erath, fixing ~50 GT of carbon into organic matter per year through photosynthesis; however, various phytoplankton taxa affect differently the carbon fixation and export (Sathyendranath et al., 2014). Chlorophyll a (Chl a), an essential phytoplankton photosynthetic pigment, has been considered a reliable indicator of phytoplankton biomass and primary productivity in aquatic systems (Bracher et al., 2015). Phytoplankton also contain several accessory pigments such as chlorophyll-b (Chl b), chlorophyll-c (Chl c), photosynthetic carotenoids (PSC) and photo-protective carotenoids (PPC) that are either involved in light harvesting, or in protecting Chl a and other sensitive pigments from photo-damage (Fishwick et al., 2006). Some of PSCs and PPCs are taxa-specific and have been considered as bio-marker pigments: e.g., fucoxanthin (PSC) for diatoms, peridinin (PPC) for certain dinoflagellates, alloxanthin (PPC) for cryptophytes, zeaxanthin (PPC) for prokaryotes (e.g. cyanobacteria), and the degradation products of Chl a, namely, divinyl Chl a and divinyl-Chl b for prochlorophyte (Jeffrey and Vest, 1997). High-Performance Liquid Chromatography (HPLC) which can efficiently detect and quantify several chemo-taxonomically significant chlorophylls and carotenoids, when coupled with these taxa-specific pigment ratios, allow phytoplankton taxonomic composition to be quantified based on a pigment concentration diagnostic procedures such as CHEMTAX (Mackey et al., 1996). Furthermore, phytoplankton pigments with distinct absorption characteristics strongly influence the light absorption by phytoplankton (Bidigare et al., 1990; Ciotti et al., 2002; Bricaud et al., 2004). As such, phytoplankton absorption spectra has been used to infer underlying pigments and also phytoplankton taxonomy by Gaussian-decomposition of (Hoepffner and Sathyendranath, 1991; Lohrenz et al., 2003; Ficek et al., 2004; Chase et al., 2013; Moisan et al., 2013; Wang et al., 2016; Moisan et al., 2017). More importantly, phytoplankton optical properties (absorption and backscattering) bearing the imprints of different pigments and cell-size, are important contributors to reflectance in a waterbody (Gordon et al., 1988). Morel and Prieur, (1977) first reported the feasibility of calculating the phytoplankton absorption coefficients and other inherent optical properties (IOPs) from measured subsurface irradiance reflectance based on the simplified radiative transfer equation. Improvements in semi-analytical inversion algorithms to derive IOPs from in-situ and remotely sensed reflectance spectra have been reported (Roesler and Perry, 1995; Hoge and Lyon, 1996; Lee et al., 1996; Garver and Siegel, 1997; Carder et al., 1999; Maritorena et al., 2002; Roesler and Boss, 2003; Chase et al., 2017). Roesler et al. (2003) further modified an earlier IOP inversion algorithm used in Roesler and Perry, (1995) by adding a set of 5 species-specific phytoplankton absorption spectra, and derived phytoplankton taxonomic composition from the field measured remote sensing reflectance.

Phytoplankton pigment composition varies not only between taxonomic groups but also with photo-physiological state of cells and environmental stress (e.g., light, nutrients, temperature, salinity, turbulence and stratification) (Suggett et al., 2009). The photosynthetic pigment field is an important factor influencing the magnitude of fluorescence emitted by phytoplankton, with active fluorometry commonly used to obtain estimates of phytoplankton biomass (D'Sa et al., 1997). Advanced active fluorometry termed as fast repetition rate (FRR; (Kolber et al., 1998)) and analogous techniques such as the fluorescence induction and relaxation (FIRe; (Suggett et al., 2008)) allows for the simultaneous measurements of the maximum PSII photochemical efficiency (F_V/F_M; where F_m and F_o is maximum and minimum fluorescence yield and F_v is variable fluorescence obtained by subtracting F_o from F_m) and the effective absorption cross section (σ_{PSII}) of a phytoplankton population; these have been used as diagnostic indicators for the rapid assessment of phytoplankton health and photo-physiological state linked to environmental stressors. Considerable effort has been invested to achieve a deeper understanding of the impacts of environmental factors and phytoplankton taxonomy on photosynthetic performance of natural communities from field and laboratory fluorescence measurements (Kolber et al., 1988; Geider et al., 1993; Schitüter et al., 1997; Behrenfeld and Kolber, 1999; D'Sa and Lohrenz, 1999;

98   Holmboe et al., 1999; Moore et al., 2003). Furthermore, knowledge of photo-physiological responses of
99   phytoplankton in combination with information on phytoplankton taxonomic composition could provide
100 additional insights on regional environmental conditions.

101 Synoptic mapping of aquatic ecosystems using satellite remote sensing has revolutionized our
102 understanding of phytoplankton dynamics at various spatial and temporal scales in response to
103 environmental variabilities and climate change. It has also provided greater understanding of biological
104 response to large events such as hurricanes in oceanic and coastal waters (Babin et al. 2004; Acker et al.
105 2009; D'Sa 2014; Farfan et al. 2014; Hu and Feng, 2016). Although the primary focus of ocean color
106 sensors has been to determine the Chl a concentration and related estimates of phytoplankton primary
107 production (Mitchell, 1994; Behrenfeld and Falkowski, 1997), more recently, several approaches have
108 been developed based on phytoplankton optical signatures to derive spatial distributions of phytoplankton
109 functional types (PFTs) (Alvain et al., 2005; Nair et al., 2008; Hirata et al., 2011), phytoplankton size
110 classification (Ciotti et al., 2002; Hirata et al., 2008; Brewin et al., 2010; Devred et al., 2011), and
111 phytoplankton accessory pigments (Pan et al., 2010; Pan et al., 2011; Moisan et al., 2013; Moisan et al.,
112 2017; Sun et al., 2017). The basis of these satellite-based remote sensing algorithms have relied on
113 distinct spectral contributions from phytoplankton community composition (e.g., taxonomy, size structure)
114 to remote sensing reflectance (R_{rs}, sr^{-1}); however, these studies have all been confined to open ocean and
115 shelf waters. In contrast, satellite studies of phytoplankton pigments have been limited in the optically
116 complex estuarine waters where the influence from wetlands, rivers, and coastal ocean make
117 phytoplankton communities highly variable and complex.

118 In this study, field bio-optical measurements and ocean color remote sensing data (Sentinel-3A OLCI)
119 acquired in Galveston Bay, a shallow estuary along the Gulf coast (Texas, USA; Fig. 1), are used to
120 investigate the spatial distribution of phytoplankton pigments, taxonomic composition, and their photo-
121 physiological state following the extreme flooding of the Houston Metropolitan and surrounding areas
122 due to Hurricane Harvey and the consequent biological impact of the floodwater discharge into the bay.
123 The paper is organized as follows: section 2 describes the field data acquisition, laboratory processing,
124 and the algorithms and methods used to distinguish phytoplankton groups, retrieve spatial distribution of
125 pigments, and calibrate phytoplankton physiological parameters. Results and discussion (sections 3 and 4),
126 and conclusions (section 5) addresses the main contributions and findings of this paper.
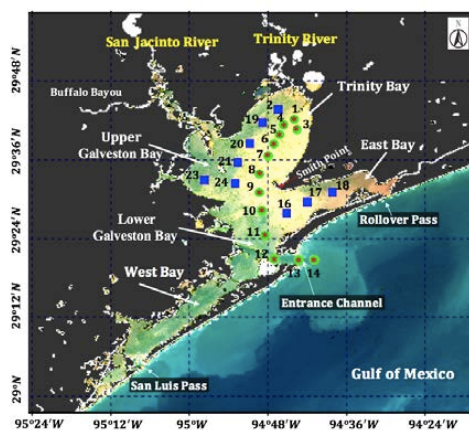
127

128 **Figure 1**. Sentinel-3A OLCI RGB image (October 29, 2017) with locations of sampling sites in
129 Galveston Bay acquired on September 29 (red asterisk), October 29 (green circles) and October 30 (blue
130 solid squares), 2017, respectively.

2. Data and Methods

2.1 Study area

Galveston Bay (GB), a shallow water estuary (~2.1 m average depth), encompasses two major sub-estuaries: San Jacinto Estuary (also divided as Upper GB and Lower GB), and Trinity Estuary (Trinity Bay) (Fig. 1). It is located adjacent to the heavily urbanized and industrialized metropolitan areas of Houston, Texas (Dorado et al., 2015). A deep (~14 m) narrow Houston Ship Channel connects the bay to the northern Gulf of Mexico (nGoM) through a narrow entrance, the Bolivar Roads Pass. Tidal exchange between GB and the nGoM occurs through the entrance channel with diurnal tides ranging from ~0.15 to ~0.5 m. The major freshwater sources to GB are the Trinity River (55%), the San Jacinto River (16%), and Buffalo Bayou (12%) (Guthrie et al., 2012). The San Jacinto River was frequently observed to transport greater amounts of dissolved nutrients into GB than the Trinity River (Quigg, 2011). The catastrophic flooding of Houston and surrounding areas associated with Hurricane Harvey resulted in strong freshwater inflows into GB from the San Jacinto River (>3300 m^3s^{-1}; USGS 8068090) on August 29, 2017 and the Trinity River (>2500 m^3s^{-1}; USGS 08066500 site at Romayor, Texas) on August 30, 2017, respectively. Although the discharge from the two rivers in the upstream returned to normal conditions (~50–120 m^3s^{-1}) in about 2 weeks after the Hurricane passage, salinity remained low for over a month following the hurricane passage (D'Sa et al., 2018).

2.2 Sampling and Data Collection

Surface water samples were collected at a total of 34 stations during two surveys on September 29 and October 29–30, 2017 (Fig. 1). Samples at stations 1 to 14 (red asterisk on top of green circle; Fig. 1) along the Trinity River transect were collected repetitively on September 29 and October 29, 2017, respectively. Additional 9 sampling sites (blue squares; Fig. 1) around the upper bay and in the East Bay were sampled on October 30, 2017. The surface water samples were stored in coolers and filtered on the same day. The filter pads were immediately frozen and stored in liquid nitrogen for laboratory absorption spectroscopic and HPLC measurements of the samples. An optical package equipped with a conductivity-temperature-depth recorder (Sea-Bird SBE) and a Fluorescence Induction and Relaxation System (FIRe; Satlantic Inc) was used to obtain profiles of salinity, temperature, pressure, and phytoplankton physiological parameters (F_V/F_M and σ_{PSII}). Measurements of backscattering were also made at each station using a WETLabs VSF-3 (470, 530, 670 nm) backscattering sensor (D'Sa et al. 2006; Naik et al. 2013). Included in the optical package was also a hyperspectral downwelling spectral irradiance meter (HyperOCR, Satlantic). The irradiance data from HyperOCR were processed using Prosoft 7.7.14 and the Photosynthetically Active Radiation (PAR) were estimated from the irradiance measurements. The above-water reflectance measurements were collected using a GER 1500 512iHR spectroradiometer in the 350-1050 nm spectral range. At each station, sky radiance, plate radiance, and water radiance were recorded (each repeated three times) and processed to obtain above-water remote sensing reflectance (Joshi et al., 2017). Sentinel-3A OLCI full resolution mode, cloud free level-1 images were obtained for September 29, October 29 and 30, 2017 over GB from the European Organization for Meteorological Satellites (EUMESAT) website and pre-processed using Sentinel-3 Toolbox Kit Module (S3TBX) version 5.0.1 in Sentinel Application Platform (SNAP). These OLCI data were further atmospherically corrected to obtain remote sensing reflectance (R_{rs_OLCI}, sr^{-1}) using Case-2 Regional Coast Color (C2RCC) module version 0.15 (Doerffer and Schiller, 2007).

2.3 Absorption Spectroscopy

Surface water samples were filtered through 0.2-μm nuclepore membrane filters and the colored dissolved organic matter (CDOM) absorbance (A_{CDOM}) were obtained using a 1-cm path length quartz cuvette on a

Perkin Elmer Lambda-850 UV/VIS spectrophotometer equipped with an integrating sphere. The Quantitative Filter Technique (QFT) with 0.7-µm GF/F filters were used to measure absorbance of particles (A_{total}) and non-algal particles (A_{NAP}) inside an integrating sphere at 1 nm intervals from 300 to 800 nm. The absorption coefficients of CDOM (a_{CDOM}), NAP (a_{NAP}), particles (a_{total}) and phytoplankton (a_{PHY}) were calculated using the following equations:

$$a_{CDOM}(\lambda) = 2.303 \times \frac{A_{CDOM}(\lambda)}{L} \qquad \text{…… (1)}$$

where L is the path length in meters. The a_{CDOM} were corrected for scattering, temperature, and baseline drift by subtracting an average value of absorption between 700-750 nm for each spectrum (Joshi and D'Sa, 2015).

$$a_{total}(\lambda) = 2.303 \times \frac{A_{total}(\lambda)}{V_{filtered}/S_{filter}} \qquad \text{…… (2)}$$

$$a_{NAP}(\lambda) = 2.303 \times \frac{A_{NAP}(\lambda)}{V_{filtered}/S_{filter}} \qquad \text{…… (3)}$$

$$a_{PHY}(\lambda) = a_{total} - a_{NAP} \qquad \text{…… (4)}$$

where $V_{filtered}$ is the filtered volume of sample, S_{filter} is the area of filter pads and the path length correction for filter pad was applied according to (Stramski et al., 2015).

2.4 Pigment Absorption Spectra

The water samples were filtered with 0.7-µm GF/F filter. The filter pads were stored in liquid nitrogen until transferred into 30 ml vials containing 10 ml cold 96% ethanol (Ritchie, 2006). The vials were spun evenly to ensure full exposure of the filter pad to the ethanol and then kept in the refrigerator (in the dark) overnight. The pigment solutions at room-temperature were poured off from vials into 1 cm cuvette and measured on a Perkin Elmer Lambda-850 UV/VIS spectrophotometer to obtain pigment absorbance spectra (A_{pig}), while, 90% ethanol was used as a blank (Thrane et al., 2015). The total absorption coefficients of pigments $a_{pig}(\lambda)$ were calculated as follow:

$$a_{pig}(\lambda) = 2.303 \times \frac{A_{pig}(\lambda)}{L} \times \left(\frac{V_{ethanol}}{V_{filtered}}\right) \qquad \text{…… (5)}$$

where L is the path length in meters, $V_{ethanol}$ is the volume of ethanol, and $V_{filtered}$ is the filtered volume of the water samples.

2.5 HPLC Measurements

Water samples were filtered through 0.7-µm GF/F filters and immediately frozen in liquid nitrogen for HPLC analysis using the methods reported by Barlow et al. (1997). The detected pigments along with their abbreviations are listed in Table 1. Diagnostic biomarker pigments are marked in bold letters (Table 1).

Table 1. Pigments information acquired from HPLC samples in Galveston Bay.

Variable	Primary Pigment (PPig)	Calculation

Chlorophylls		
[TChl a]	Total chlorophyll a (TChl a)	[Chlide a]+[DVChl a]+[Chl a]
[TChl b]	Total chlorophyll b (TChl b)	[DVChl b]+**[Chl b]**
[TChl c]	Total chlorophyll c (TChl c)	[Chl c_1]+[Chl c_2]+[Chl c_3]
Carotenoids		
[Caro]	Carotenes†	[ββ-Car]+[βε-Car]
[Allo]	**Alloxanthin**	
[Buta]	**19'-Butanoyloxyfucoxanthin**	
[Diadino]	Diadinoxanthin	
[Diato]	Diatoxanthin	
[Fuco]	**Fucoxanthin**	
[Hexa]	**19'-Hexanoyloxyfucoxanthin**	
[Peri]	**Peridinin**	
[Zea]	**Zeaxanthin**	
[Neo]	Neoxanthin	
[Lut]	Lutein	
[Viola]	Violaxanthin	
[Pras]	Prasinoxanthin	
[Anthera]	Antheraxanthin	

Note: (1) [Chl b], [Allo], [Fuco], [Peri], [Zea], [Buta] and [Hexa] are considered as diagnostic pigments for PFTs (Moisan et al., 2017).

Variable	Pigment Sum	Calculation
[TChl]	Total Chlorophyll (TChl)	[TChl a]+[TChl b]+[TChl c]
[PPC]	Photoprotective Carotenoids (PPC)	[Allo]+[Diadino]+[Diato]+[Zea]+[Caro]+[Viola]
[PSC]	Photosynthetic Carotenoids (PSC)	[Buta]+[Fuco]+[Hexa]+[Peri]+[Lut]+[Pras]
[PSP]	Photosynthetic Pigments (PSP)	[PSC]+[TChl]
[AP]	Total Accessory Pigments (AP)	[PPC]+[PSC]+[TChl b]+[TChl c]
[TP]	Total Pigments (TP)	[AP]+[TChl a]
[DP]	Total Diagnostic Pigments (DP)	[PSC]+[Allo]+[Zea]+[T Chl b]

206 **2.6 FIRe Measurements**

207 An in-situ Fluorescence Induction and Relaxation System (FIRe, Satlantic Inc.) was used to characterize
208 phytoplankton photosynthetic physiology during the two surveys in GB. The FIRe is based on
209 illuminating a sample with an intense flash of light to instantaneously saturate the reaction centers of
210 photosystem II (PSII); under these light conditions, reaction centers do not accept electrons and most of
211 the absorbed light energy is dissipated as fluorescence. The fundamental parameter measured by FIRe is
212 fluorescence yield F(t), which is the emitted fluorescence divided by the irradiance intensity (no unit). In
213 contrast to strong flashes, dark adaption enables all reaction centers of PSII to be open with least
214 fluorescence emitted, thus, resulting in minimal fluorescence yield (F_o). Maximum fluorescence yield (F_m)
215 can be obtained after sufficient irradiation when all reaction centers are closed. Maximum photochemical
216 efficiency, which quantify the potential of converting light to chemical energy for the PSII reaction
217 centers (Moore et al., 2006), was calculated as $(F_m - F_o)/ F_m = F_v / F_m$. The functional absorption cross
218 section σ_{PSII} ($Å^2 quantum^{-1}$) measures the capability of reaction centers to absorb light from the ambient
219 environment. The FIRe was deployed at a slow descent rate, with 12 and 20 vertical profiles obtained
220 during the first and second surveys, respectively. All measurements were programmed using standard

221 protocols of single saturating turn-over (ST) flash saturation of PSII (Kolber et al., 1998). Flashes were
222 generated from highly uniform blue LEDs at 455 nm with approximately 30 nm half-bandwidth. Chl a
223 fluorescence was stimulated using saturating sequence of 80 1.1 μs flashes applied at 1 μs intervals, 8
224 sequences were averaged per acquisition, and the fluorescence signal was detected at 668 nm. All data
225 were processed using standard FIReCom software (Satlantic). In addition, samples of 0.2-μm filtered sea
226 water at each station were used as 'blank' to remove the background fluorescence signals (Cullen and
227 Davis, 2003); in this step, the fluorescence from the filtered samples (without phytoplankton) were
228 subtracted from in-situ fluorescence signals to get more accurate values of F_v/F_m.

229 **2.7 Retrieving Phytoplankton Groups from above-water R_{rs}**

230 A fundamental relationship that links sub-surface remote-sensing reflectance (r_{rs}) and the IOPs was
231 expressed using a quadratic function developed by (Gordon et al., 1988):

232 $$r_{rs} = g_1 * u(\lambda) + g_2 * u(\lambda)^2; \ u(\lambda) = \frac{b_b}{a_{total}+b_b} \qquad \ldots\ldots (6)$$

233 where, the parameters g_1 (~0.0788) and g_2 (~0.2379) are values for turbid estuarine waters (Joshi and
234 D'Sa, 2018); r_{rs} is the sub-surface remote sensing reflectance that were obtained from above-water remote
235 sensing reflectance (R_{rs}) using (Lee et al., 2002):

236 $$r_{rs} = \frac{R_{rs}}{0.52+1.7 \times R_{rs}} \qquad \ldots\ldots (7)$$

237 The total backscattering coefficient b_b is comprised of water (b_{bw}) and particulates including both organic
238 and inorganic particles (b_{bp}), while the total absorption coefficients (a_{total}) can be further separated into
239 four sub-constituents (Roesler and Perry, 1995) as indicated by:

240 $$b_b = b_{bw} + b_{bp}; \ a_{total} = a_w + a_{phy} + a_{CDOM} + a_{NAP} \qquad \ldots\ldots (8)$$

241 where a_w, a_{phy}, a_{CDOM}, and a_{NAP} represent the absorption coefficients of pure water, phytoplankton,
242 colored dissolved organic matter and non-algal particles, respectively.

243 The IOP inversion algorithm for retrieving IOPs from R_{rs} require known spectral shape (eigenvector) of
244 each component in Eq. (8) to estimate the magnitude (eigenvalue) of each component (Table 2). The
245 spectral shape can be adjusted by changing the values of slope based on characteristics of the study area.
246 It is worth noting that a single averaged phytoplankton eigenvector does not provide species information
247 whereas a set of several species-specific phytoplankton eigenvectors allow estimates of species
248 composition. IOPs inversion algorithm applied in this study makes use of mass-specific phytoplankton
249 absorption spectra of 10 groups namely, dinoflagellate, diatom, chlorophyte, cryptophyte, haptophyte,
250 prochlorophyte, raphidophyte, rhodophyte, red cyanobacteria (*Synechococcus*) and blue cyanobacteria
251 (*Trichodesmium*); these were obtained from Dierssen et al. (2006) and Dutkiewicz et al. (2015) as eigen
252 vectors rather than using one average $a_{phy}(\lambda)$ spectrum. Subsequently, the inversion algorithm iterates
253 repeatedly to minimize the difference between modeled R_{rs} and in-situ measured R_{rs} (R_{rs_insitu}) until a best
254 fit is achieved while allowing for alterations of all parameters listed in Table 2 (Chase et al., 2017). The
255 absolute percent errors between modeled and measured values of R_{rs}, a_{phy}, a_{CDOM}, a_{NAP} and b_{bp} were
256 calculated as:

257 $$\%error = \left|\frac{x_{modeled}-x_{measured}}{x_{measured}}\right| \times 100 \qquad \ldots\ldots (9)$$

258 **Table 2.** Parameters and eigenvectors used in the semi-analytical inversion algorithm.

Parameter	Equation	Slope	Eigenvalue
$a_{CDOM}(\lambda)$	$a_{CDOM}(\lambda) = M_{CDOM} \times \exp^{-S_{CDOM} \times (\lambda - \lambda_0)};$ $\lambda_0 = 443$	S_{CDOM}	M_{CDOM}
$a_{NAP}(\lambda)$	$a_{NAP}(\lambda) = M_{NAP} \times \exp^{-S_{NAP} \times (\lambda - \lambda_0)};$ $\lambda_0 = 443$	S_{NAP}	M_{NAP}
$a_{phy}(\lambda)$	$a_{phy}(\lambda) = \sum Chl\ a_i \times a_{phi}^*;$ a_{phi}^* is the spectral shape of each phytoplankton group.		$Chl\ a_i$
$b_{bp}(\lambda)$	$b_{bp}(\lambda) = B_{bp} \times (\lambda_0/\lambda)^{S_{bp}};$ $\lambda_0 = 443$	S_{bp}	B_{bp}
Note: $a_{phi}^*(\lambda)$ for 10 different groups of phytoplankton used in this study were extracted from (Dierssen et al., 2006) and Dutkiewicz et al., (2015).			

259 **2.8 Retrieving Pigments from Sentinel 3-OLCI R_{rs}**

260 **2.8.1 Reconstruction of Pigment Absorption Spectrum by Multiple Linear Regression**

261 Total pigment absorption spectra $a_{pig}(\lambda)$ obtained during both surveys (Eq. 5), were modeled as a third
262 order function of HPLC measured Chl a (Chl a_HPLC) concentration at each station as (Moisan et al., 2017):

263
$$a_{pig}(\lambda) = C_3 \times (Chl\ a_{\_HPLC})^3 + C_2 \times (Chl\ a_{\_HPLC})^2 + C_1 \times Chl\ a_{\_HPLC} + C_0 \quad \ldots\ldots (11)$$

264 where C=$[C_3, C_2, C_1, C_0]$, is the wavelength-dependent vector coefficient ranging from 400 to 700 nm at
265 1 nm interval; these were further applied to Sentinel-3A OLCI Chl a to calculate a_{pig_OLCI} at each pixel as:

266
$$a_{pig\_OLCI}(\lambda) = C_3 \times (Chl\ a_{\_OLCI})^3 + C_2 \times (Chl\ a_{\_OLCI})^2 + C_1 \times Chl\ a_{\_OLCI} + C_0 \quad \ldots\ldots (12)$$

267 where Chl a_OLCI is Sentinel-3A OLCI derived Chl a concentration (259×224 pixels); the obtained image
268 represents the value of a_{pig_OLCI} at a certain wavelength and 301 images of a_{pig_OLCI} can be obtained in
269 the 400-700 nm wavelength range at 1 nm interval.

270 **2.8.2 Satellite Retrieval of Pigments using Non-Negative Least Square (NNLS) Inversion Model**

271 The a_{pig_OLCI} is a mixture of n pigments with known absorption spectra $a_i(\lambda)$, $i = 1,2,\ldots,n$ at wavelength
272 λ (nm); thus, $a_{pig\_OLCI}(\lambda)$ can be considered as a weighted sum of individual component spectrum
273 (Thrane et al., 2015) at each image point as:
274
275
$$a_{pig\_OLCI}(\lambda) = x_1 \times a_1(\lambda) + x_2 \times a_2(\lambda) + \cdots x_n \times a_n(\lambda) \quad \ldots\ldots (13)$$
276
277 where $A(\lambda) = [a_1(\lambda), a_2(\lambda), \ldots a_n(\lambda)]$ are the spectra of 16 pigments (Chl a, Chl b, Chl c_1, Chl c_2,
278 pheophytin-a, pheophytin-b, peridinin, fucoxanthin, neoxanthin, lutein, violaxanthin, alloxanthin,
279 diadinoxanthin, diatoxanthin, zeaxanthin, and β-carotenoid) extracted from supplementary R scripts of
280 Thrane et al. (2015). All these 16 spectra are normalized to unit maximum peak absorbing value. The
281 vector coefficient $[x_1, x_2, \ldots x_n]$ correspond to the weights of these distinct pigments; note that X cannot be
282 negative, therefore, non-negative least squares (NNLS) was used to guarantee positive solutions of X
283 (Moisan et al., 2013; Thrane et al., 2015). Eq. 13 can be further expressed as:

284

285
$$\begin{bmatrix} a_{pig}(400)_{OLCI} \\ a_{pig}(401)_{OLCI} \\ \vdots \\ a_{pig}(700)_{OLCI} \end{bmatrix} = \begin{bmatrix} x_1 \\ x_2 \\ \vdots \\ x_n \end{bmatrix} \times \begin{bmatrix} a_1(400), a_2(400), \dots a_n(400) \\ a_1(401), a_2(401), \dots a_n(401) \\ \vdots \\ a_1(700), a_2(700), \dots a_n(700) \end{bmatrix} \quad \dots\dots (14)$$

286
287 where n=16 is the number of pigment components included in the NNLS inversion model and x_n is the
288 weight mentioned above for the nth pigment. Note: x_n is not the concentration of each pigment component;
289 the concentration of pigments (C_n, µg L^{-1}) were further calculated by dividing the pigment's weight-
290 specific absorption coefficient (U_n, L g^{-1}cm^{-1}) at maximum peak wavelength (Thrane et al., 2015) as:

291
$$C_n = 10000 \times \left(\frac{X_n}{U_n}\right) \quad \dots\dots (15)$$

292 **2.9 Processing Approach**

293 Sentinel 3A-OLCI pigment maps were generated using the processing pathway 1 (Fig. 2) that includes the
294 following: 1) developing empirical relationships between HPLC-measured Chl a and R_{rs_insitu} band ratio
295 for Sentinel 3A-OLCI band 9 (673 nm) and band 11 (709 nm) to generate Sentinel 3A-OLCI Chl a maps,
296 2) converting Chl a concentration to $a_{pig\_OLCI}(\lambda)$ maps, and subsequently decomposing $a_{pig\_OLCI}(\lambda)$ into
297 individual pigment spectra to generate phytoplankton pigment maps for GB. In processing pathway 2,
298 phytoplankton taxonomic composition at each sampling station was obtained from a 10-species IOP
299 inversion model, which take R_{rs_insitu} as input and estimates Chl a concentration of each phytoplankton
300 group (Fig. 2). Finally, CDOM-corrected FIRe measurements of F_v/F_m and σ_{PSII} were combined with
301 phytoplankton taxonomy to assess photosynthetic physiology of different phytoplankton groups.

302
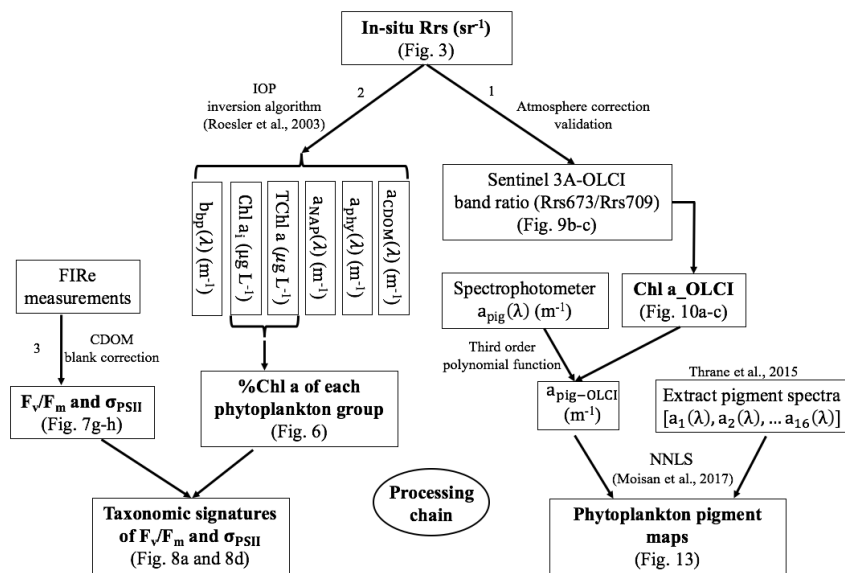
303 **Figure 2.** Flowchart showing the three processing steps for: (1) retrieving pigments spatial distribution
304 maps from OLCI, (2) distinguishing phytoplankton groups, and (3) assessing phytoplankton physiological
305 parameters and their linkages to taxonomic groups.

3. Results

3.1 Phytoplankton Taxonomy and Physiological State from Field Observations

3.1.1 Measurements of Above Water Remote Sensing Reflectance

Above-water remote sensing reflectances (R_{rs_insitu}) from the two surveys (Fig. 3) reflect the influence of the absorbing and scattering features of water constituents. Low reflectance (~675 nm) caused by Chl a red light absorption and maximum reflectance at green wavelength (~550 nm) were observed. Obvious dips at ~625 nm versus reflectance peaks ~650 nm were observed in spectra during both surveys, which could be attributed to cyanobacteria (*Trichodesmium*) modulation of the spectra (Hu et al., 2010). The reflectance peak around 690–700 nm was obvious at most sampling sites except at stations 13 and 14 adjacent to the nGOM and were likely due to the suspended sediment scattering and effect of Chl a fluorescence (Gitelson, 1992). The peak position at stations with lower Chl a concentration (~5 µg L^{-1}) were observed at 690-693 nm; however, the peaks shifted to longer wavelengths of 705 and 710 nm for station 23 and 19 with extremely high Chl a concentrations of ~31 and 50 µg L^{-1}, respectively (Fig. 3).
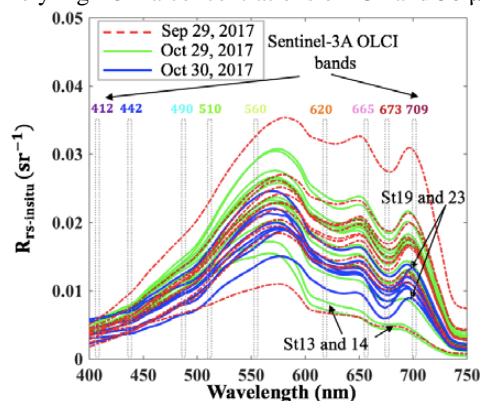
Figure 3. R_{rs_insitu} spectra at stations in GB on September 29, and October 29-30, 2017; vertical bars represent Sentinel-3A OLCI spectral bands.

3.1.2 Performance of IOP Inversion Algorithm

The IOP inversion algorithm was applied to R_{rs_insitu} data (Fig. 3) obtained during the two surveys in GB. The mean errors for modeled a_{CDOM}, a_{NAP}, a_{phy} and b_{bp_470} at all wavelengths for the 34 stations were 5.86%, 6.83%, 12.19% and 10.79%, respectively (Table 3). A total of 8 phytoplankton groups (dinoflagellate, diatom, chlorophyte, cryptophyte, haptophyte, prochlorophyte, raphidophyte, and blue cyanobacteria) were spectrally detected from the IOP inversion algorithm. The sum of 8 eigenvalues of Chl_i (Table 2) represents the modeled total Chl a (TChl $a_{\_mod}$) of the whole phytoplankton community. The TChl $a_{\_mod}$ is better correlated with HPLC-measured total Chl a (TChl a_{HPLC}) for survey 2 (green circle; Fig. 4a) with $R^2 \sim 0.92$, compared to survey 1 (red color; Fig. 4a). In addition, the TChl $a_{\_mod}$ appear to be slightly higher than TChl a_{HPLC} for survey 2. The modeled a_{CDOM} (a_{CDOM_mod}) are in close agreement with spectrophotometrically measured a_{CDOM} at 412 nm (Fig. 4b), with a_{CDOM} obtained on September 29, 2017 much higher than that on October 29-30, 2017. The modeled b_{bp} (b_{bp_mod}) are well correlated with in-situ b_{bp} (b_{bp_insitu}) at 470 nm (Fig. 4c) with higher R^2 (0.81) observed on September 29, 2017. In addition, both modeled and field-measured b_{bp} showed stronger backscattering at most stations on September 29, 2017 than those on October 29-30, 2017.

Table 3. Error statistics over all wavelengths and sampling stations (N=301×34=10234; 12 and 22 stations on Sep 29 and Oct 29-30, 2017) from semi-analytical IOP inversion algorithm.

Parameter	Min. error (%)	Max. error (%)	Mean error (%)	R^2(Sep)	R^2(Oct)
R_{rs} $\lambda \in [400,700]$	0.005	40.12	18.71	0.90	0.89
$a_{CDOM}(\lambda)$, $\lambda \in [400,700]$	0.042	11.20	5.86	0.92	0.94
$a_{NAP}(\lambda)$, $\lambda \in [400,700]$	0.001	11.46	6.73	0.90	0.91
$a_{PHY}(\lambda)$, $\lambda \in [400,700]$	0.001	36.42	12.19	0.84	0.85
$b_{bp}(\lambda)$, $\lambda = 470$ nm	0.057	40.22	10.79	0.81	0.43

The Chl a percentage (%Chl a), which is Chl_i/TChl a, were also compared with diagnostic pigment percentage (%DP), which is specific DP for each phytoplankton group over the sum of DP ($\sum$ DP). The DP for diatom (fucoxanthin), dinoflagellate (peridinin), cryptophytes (alloxanthin), chlorophyte (Chl b), haptophyte (19'-hexanoyloxyfucoxanthin), and cyanobacteria (zeaxanthin) referred in (Moisan et al., 2017) were used in this study. The R^2 between %Chl a and %DP for different phytoplankton groups range from 0.15 to 0.81 (Fig. 4). The %Chl a of cryptophyte is between 5%-42% and well correlated with alloxanthin/$\sum$ DP (R^2~0.62-0.72; Fig. 4d) for both surveys. In addition, the cryptophyte %Chl a at station 19 and 23 on October 30, 2017 was highest (~40%) in coincidence with the highest value of alloxanthin/$\sum$ DP (Fig. 4d). Furthermore, relationship between chlorophyte %Chl a and Chl b/$\sum$ DP (R^2~0.55; Fig. 4e) showed that chlorophyte during survey 1 contributed higher fraction to the whole phytoplankton community compared to survey 2. The %Chl a of cyanobacteria highly correlated with zeaxanthin/$\sum$ DP with R^2 larger than 0.7 (Fig. 4f) for both surveys. Low %Chl a of dinoflagellate in coincidence with low peridinin/$\sum$ DP (R^2~0.78) were observed at stations along the transect, however, increased contribution of dinoflagellate appeared adjacent to the entrance during both surveys (Fig. 4g).
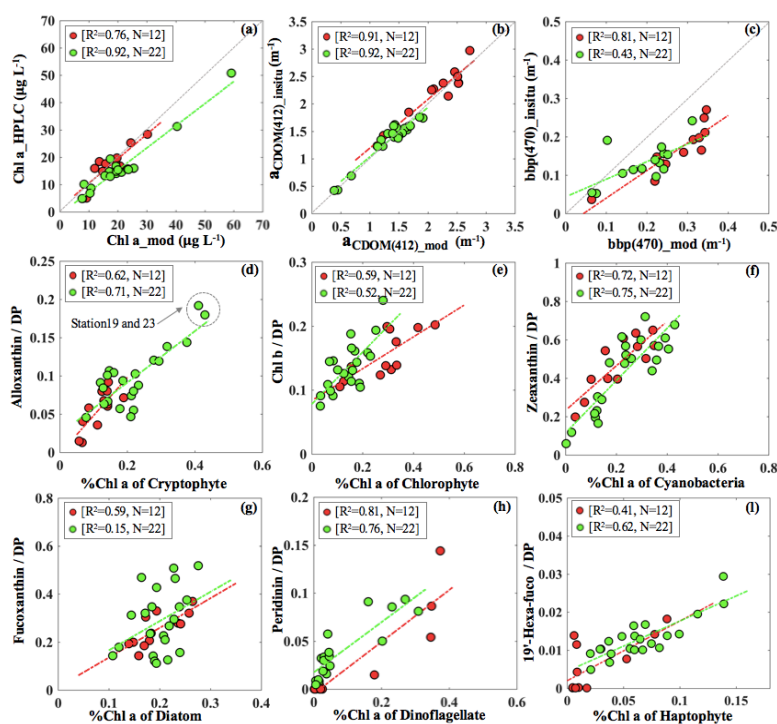
357 **Figure 4.** (a) Validation of TChl a_mod via HPLC-measured TChl a; individual %Chl a of each detected
358 taxa versus corresponding %DP shown with (d) cryptophyte, (e) chlorophyte, (f) cyanobacteria, (g)
359 diatom, (h) dinoflagellate, and (l) haptophyte; red and green dots indicate the samples on September 29
360 and October 29-30, 2017, respectively. Comparison between in-situ measurements and modeled results
361 with (b) $a_{CDOM}(412)$ and (c) $b_{bp}(470)$.

362 **3.1.3   Variations in Phytoplankton Community Structure**

363 Reconstruction of the phytoplankton absorption coefficients spectra revealed variations in phytoplankton
364 community structure (Fig. 5) even several weeks after Hurricane Harvey. The modeled a_{phy} spectra
365 (a_{phy_mod}) at stations 6, 13, 17 and 19 (Fig. 5a-f) yielded spatiotemporal differences of phytoplankton
366 taxonomic composition in GB. The strong absorption peak around 625 nm induced by cyanobacteria was
367 observed at most of the stations for both modeled results and in-situ measurements (Fig. 5a, 5c and 5e)
368 except at stations adjacent to the entrance (Fig. 5b and d). The a_{phy_mod} at station 6 was primarily
369 dominated by group of cyanobacteria (blue line) and chlorophyte (green line) on September 29, 2017 (Fig.
370 5a); in contrast, the spectrum of chlorophyte contributed very little at station 6 on October 29, 2017
371 (green line; Fig. 5c). Furthermore, the shape of spectra for samples obtained at station 13 showed strong
372 dinoflagellate-modulation versus extremely low cyanobacteria contribution during survey 1 (red line; Fig.
373 5b). However, small-size group like haptophyte and prochlorophyte displayed increasing proportions at
374 station 13 on October 29, 2017 (Fig. 5d). Station 17 in the East Bay was dominated by cyanobacteria
375 (blue line; Fig. 5e) and cryptophyte (pink line; Fig. 5e) absorption spectra, whereas, on October 30, 2017,
376 the main spectral features at station 19 in the upper GB was from cryptophyte (pink line) and chlorophyte
377 (green line; Fig. 5f).
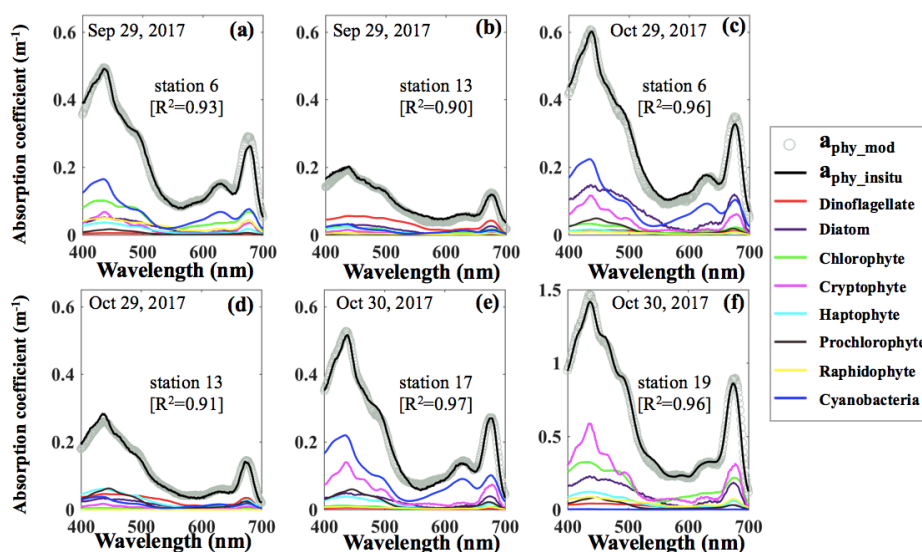
378
379 **Figure 5**. Reconstruction of phytoplankton absorption coefficients spectra at station 6 **(a)** and 13 **(b)** on
380 September 29, 2017, at station 6 **(c)** and 13 **(d)** on October 29, 2017 and at 17**(e)**, and 19 **(f)** on October
381 30, 2017 based on the mass specific absorption spectra of different phytoplankton groups including
382 diatom, chlorophyte, dinoflagellate, cryptophyte, cyanobacteria (blue), haptophyte, prochlorophyte and
383 raphidophyte presented using different colors.

384
385 The corresponding taxa-specific %Chl a derived from IOPs inversion algorithm for the two surveys on
386 September 29 and October 29-30, 2017 are shown in Figure 6a and 6b, respectively. Cyanobacteria (blue

bars) and chlorophyte (green bars) constituted over 55% of the phytoplankton communities during survey 1 (September 29, 2017; Fig. 6a). In addition, chlorophyte, known to proliferate in freshwater environments, showed higher fraction than that observed in survey 2 (green color; Fig. 6). Also, chlorophyte together with diatoms (purple color; Fig. 6a) accounted for ~ 60% of TChl a$_{mod}$ at stations (e.g., station 7, 8 and 9) with a well-mixed water column (inferred from salinity profiles; not shown) on September 29, 2017. Cryptophyte, haptophyte and raphidophyte became a minor component of the community and accounted in total to ~25% of TChl a$_{mod}$ (Fig. 6a). Furthermore, dinoflagellate group had low contributions to TChl a$_{mod}$ inside the bay, but showed increasing %Chl a (~30%) in higher salinity waters adjacent to the nGOM (red color; Fig. 6a). Cyanobacteria (blue color; Fig. 7) exhibited a slightly elevated percentage during survey 2 (~60 days after hurricane passage, October 29-30, 2017) and were quite abundant at station 16, 17 and 18 in East Bay where the water was calm and stratified as observed from salinity profiles. In addition, cyanobacteria were not prevailing adjacent to the nGOM (Station 12, 13 and 14) and close to San Jacinto (station 19, 20, 21, 23 and 24), where cryptophyte (pink color) and chlorophyte (green color) showed dominance (Fig. 6b). The %Chl a of chlorophyte obtained at stations along the Trinity River transect decreased by ~10% on October 29-30, 2017 compared to that on September 29, 2017. Small size groups like haptophyte and prochlorophyte increased on October 29-30, 2017 and were more abundant adjacent to the nGOM, accounting for more than 25% of the TChl a$_{mod}$.
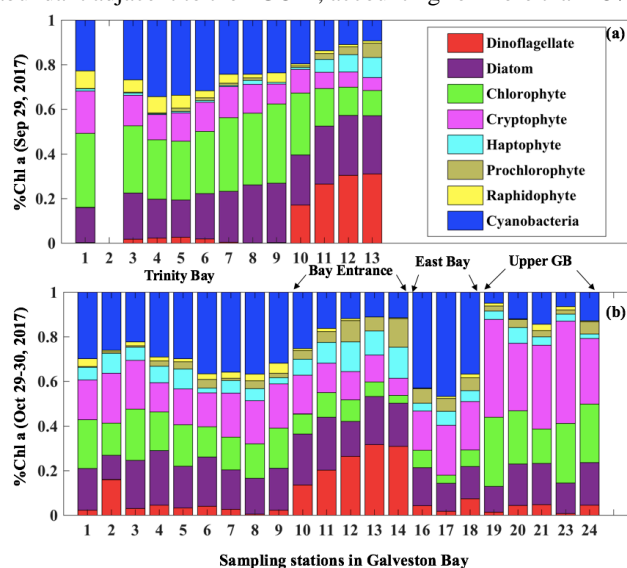
Figure 6. Phytoplankton taxonomic compositions detected from IOP inversion algorithm on September 29 and October 29-30, 2017 in Galveston Bay; phytoplankton groups are represented in different colors as shown in the legend.

3.1.4 Environmental Conditions and Physiological State of Phytoplankton Community

The surface salinity presented a pronounced seaward increasing gradient along the transect (station 3-14) during both the surveys (Fig. 7a) with primarily lower salinity throughout the bay during survey 1 in comparison to survey 2, which indicated the freshening impact was still ongoing even 4 weeks after Hurricane Harvey. The salinity was ~15 at station 16 and decreasing when going further into East Bay (~10 at station 17 and 18; Fig. 7a). In upper GB, salinity at station 19-24 did not vary significantly (~15), increasing along with the distance away from the San Jacinto River mouth with highest value (~17.5) at station 24. During both surveys, lowest Chl a (Fig. 7b) were observed adjacent to the nGOM, and the highest Chl a were closest to the river mouth. The Photosynthetically Active Radiation (PAR) which were

417 calculated from down-welling irradiance (not shown) decreased significantly with depth, but surface PAR
418 (Fig. 7c) were similar in magnitude at all stations. Pigment ratios including TChl a/TP (0.58-0.68),
419 PSC/Chl a (0.07-0.26) and AP/TP (0.34-0.42) were obtained from HPLC measurements and shown in
420 Figure 7d, 7e and 7f, respectively.

421 The CDOM calibrated and 0-0.5m depth averaged photosynthetic parameters F_V/F_M varied from 0.41 to
422 0.64 (Fig. 7g), while σ_{PSII} was in the range of 329-668 Å^{2}quantum^{-1}(Fig. 7h). The highest σ_{PSII} and
423 lowest F_V/F_M appeared adjacent to the nGOM (station 12-14). Conversely, values of F_V/F_M at stations 7-
424 9 with a well-mixed water column were high with low values of σ_{PSII}. Both F_V/F_M and σ_{PSII} did not
425 directly correlate with Chl a, (e.g., high Chl a ~51 µg L^{-1} at station 19 corresponded to a relatively low
426 level of F_V/F_M ~0.45, versus high σ_{PSII} ~550 Å^{2}quantum^{-1}). However, the stations with high F_V/F_M
427 coincided with the high fraction of Chl a (Chl a/TP) and low fraction of AP (AP/TP) (Fig. 7d and 7f). In
428 contrast, σ_{PSII} showed an overall positive relationship with AP/TP, but altered negatively with Chl a/TP
429 during both surveys. The lowest (highest) value of σ_{PSII} (F_V/F_M) were observed at station 9
430 corresponding to the highest Chl a/TP value (~0.64) on October 29, 2017. The highest AP/TP and
431 PSC/Chl a were obtained from stations adjacent to the nGOM.

432
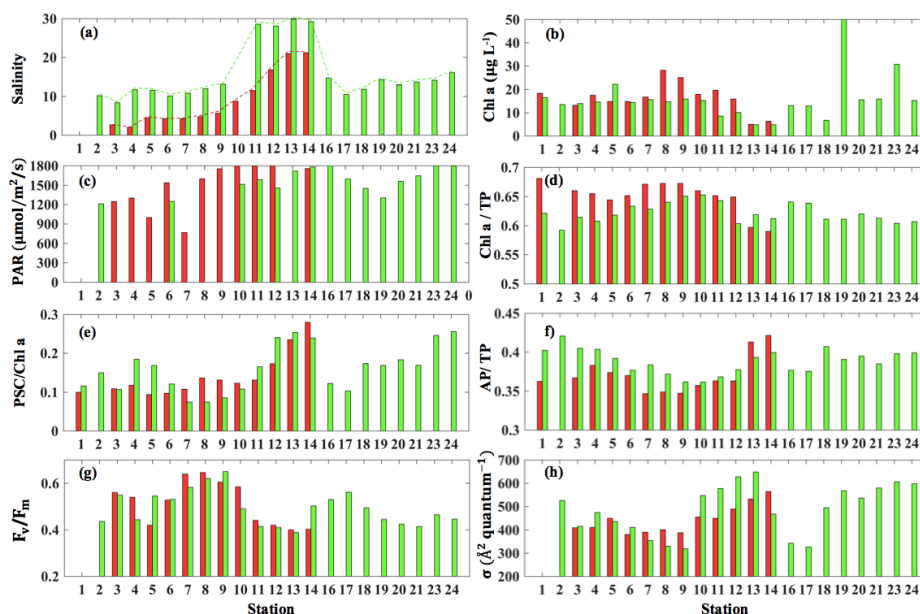
Figure 7. Environmental conditions (salinity, light field), pigment composition and physiological state in
GB surface waters (red bars indicating samples from September 29, 2017 and blue bars representing
samples from October 29 and 30, 2017). **(a)** Salinity, **(b)** Chl-a concentration, **(c)** PAR, **(d)** Chl a/TP, **(e)**
PSC/Chl a, **(f)** AP/TP, **(g)** F_v/F_m, and **(h)** σ_{PSII}.

437 **3.1.5 F_v/F_m and σ_{PSII} Taxonomic Signatures**

438 Distinct pigments housed within phytoplankton light-harvesting antennae can strongly influence PSII
439 light-harvesting capability and the photosynthetic quantum efficiency of phytoplankton (Lutz et al., 2001).
440 In this study, we observed an inverse relationship (R^2 ~0.63-0.81; Fig. 8a and d) between the F_V/F_M and
441 σ_{PSII}, that appeared related to taxonomic signals during surveys 1 and 2 in GB. Stations 1-9 along the

442 transect were considered as well-mixed group with no dominance by any particular group (black circles;
443 Fig. 8a-c); stations 10-14 close to the entrance were however, strongly dominated by dinoflagellate and
444 haptophyte (red symbol; Fig. 8a-c) during survey 1. This well-mixed group displayed low values of σ_{PSII}
445 (~390-439 Å^{2}quantum^{-1}), and high levels of F_V/F_M (~0.42-0.65) with F_V/F_M approaching 0.65 at
446 station 9 on September 29, 2017 (Fig. 8a). However, enhanced contributions of dinoflagellate and
447 haptophyte around the entrance corresponded to a decline of F_V/F_M (0.3~0.4) against an increase of σ_{PSII}
448 (500~600 Å^{2}quantum^{-1}) during survey 1. Furthermore, samples obtained from survey 2 at station 1-9,
449 station 10-14, station 16-18 and station 19-24 were considered as well-mixed (black), dinoflagellate-
450 haptophyte dominated (red), cyanobacteria dominated (blue) and cryptophyte-chlorophyte dominated
451 (green), respectively. Stations 16-17 dominated by cyanobacteria (blue triangles; Fig. 8d) showed high
452 level of F_V/F_M (0.5~0.6) and relatively low values of σ_{PSII} (300~400 Å^{2}quantum^{-1}). The F_v/F_m and
453 σ_{PSII} of cryptophyte-chlorophyte dominated stations showed a moderate level of F_V/F_M (0.4~0.5) and
454 σ_{PSII} (580~680 Å^{2}quantum^{-1}). More importantly, tight positive relationships existed between
455 measurements of F_V/F_M and Chl a/TP (R^2~0.31-0.63; Fig. 8b and e). On the other hand, σ_{PSII} were
456 positively correlated with PSC/Chl a with R^2~0.6 (Fig. 8c and f). The PSC/Chl a of cyanobacteria
457 dominated group (blue symbols), and well mixed group (brown symbols) were relatively low. Highest
458 PSC/Chl a and lowest Chl a/TP was observed for the dinoflagellate-haptophyte dominated group,
459 corresponding to the lowest σ_{PSII} and highest F_V/F_M. In addition, cryptophyte-chlorophyte dominated
460 group had high levels of PSC/TChl a (~0.18-0.26) and slightly higher Chl a/TP compared to
461 dinoflagellate-haptophyte dominated group. Overall, well-mixed groups with high proportion of large-
462 size phytoplankton (e.g., diatoms and chlorophyte) showed higher Chl a/TP along with larger F_V/F_M and
463 smaller σ_{PSII} than those stations with high fraction of dinoflagellate and pico-populations (Fig. 8c and f).
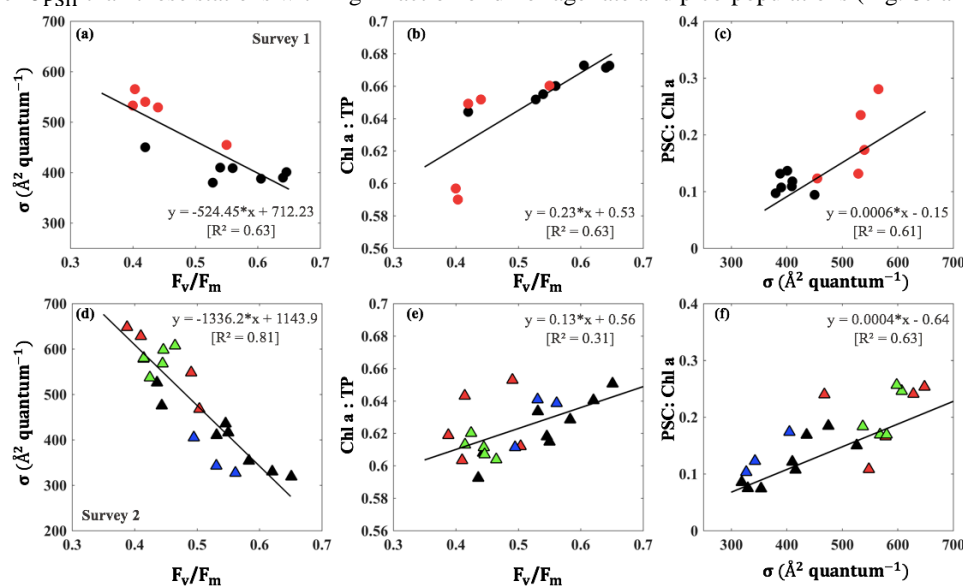
464
465 **Figure 8**. **a**, **d**) σ_{PSII} against F_V/F_M; **b**, **e**) F_V/F_M versus Chl a/TP; and **c**, **f**) σ_{PSII} versus PSC/Chl a on
466 September 29 and October 29-30, 2017 respectively. The data points identified by dominant taxa with
467 black, red, green and blue symbols denoting well-mixed, dinoflagellate-haptophyte dominated,
468 cryptophyte-chlorophyte dominated, and cyanobacteria dominated groups, respectively.

469 **3.2 Satellite Observations of Phytoplankton Pigments**

470 **3.2.1 An OLCI Chl a Algorithm and its Validation**

471 Blue to green band ratio algorithms have been widely used to study Chl a in the open ocean and shelf
472 waters (D'Sa et al., 2006; Blondeau-Patissier et al., 2014); however, these bands generally fail in
473 estuarine waters due to strong blue absorption by the high levels of CDOM and suspended particulate
474 matter, especially after flooding events associated with hurricanes (D'Sa et al., 2011; D'Sa et al., 2018;
475 Joshi and D'Sa, 2018). The percentage contribution by CDOM fluorescence (blank) to maximum
476 fluorescence yield (F_m) obtained from in-situ FIRe (Fig. 9a) demonstrated that Chl a fluorescence was
477 strongly influenced by high amounts of CDOM fluorescence in GB, especially during the first survey
478 (September 29, 2017), when the bay was under strong floodwater influence (red triangles; Fig. 9a). The
479 CDOM fluorescence signal constituted ~ 25 % in the region adjacent to the nGOM (stations 12-14),
480 between 25%-50% in the upper GB, and up to ~65% in Trinity Bay, which implied that blue and even
481 green band are highly contaminated by CDOM and might not be the most suitable bands for estimating
482 Chl a in GB. However, an increase in peak height near 700 nm and its shift towards longer wavelength
483 (Fig. 3) can be used as a proxy to estimate Chl a concentration.

484
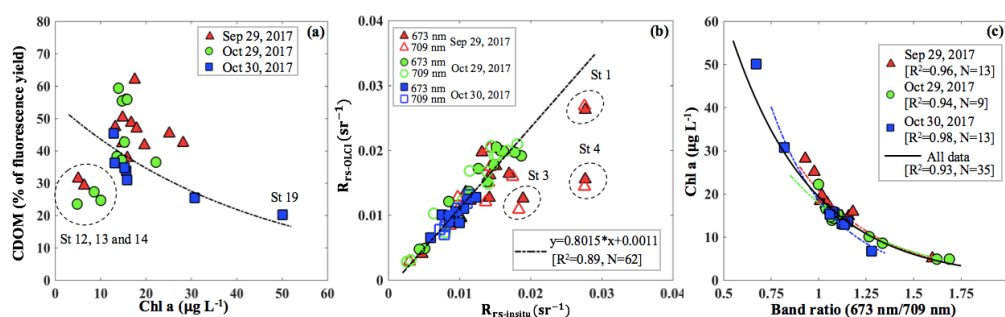
485 **Figure 9. (a)** Relationship between the percentage of the fluorescence yield of CDOM measured by FIRe
486 against HPLC measured Chl a concentration. **(b)** Comparisons between R_{rs_insitu} and R_{rs_OLCI} at band 9
487 (673 nm) and band 11 (709 nm). **(c)** Exponential relationships between HPLC-measured Chl a
488 concentrations and R_{rs_insitu} band ratio (673 nm/709 nm) in GB on September 29 (R^2=0.89), October 29
489 (R^2=0.93) and October 30 (R^2=0.97). Red, green and blue lines and symbols indicate data sets obtained on
490 September 29, October 29 and 30, 2017, respectively.

491 The C2RCC atmospheric-corrected R_{rs_OLCI} at each of the sampling sites were further averaged (3×3
492 pixels) and compared with R_{rs_insitu} (Fig. 3) at phytoplankton red absorption (~673 nm) and Chl a
493 fluorescence (~700 nm) bands (Fig. 9b). The C2RCC performed overall better for the second survey on
494 October29-30, 2017 (green and blue symbols; Fig. 9b) than the first survey on September 29, 2017 (red
495 triangles; Fig. 9b) when stations 1, 3 and 4 (circled triangles; Fig. 3c) adjacent to the Trinity River mouth
496 were included; these stations were the last sampling sites in the afternoon (~4:30 pm) and under
497 somewhat cloudy conditions. The time difference between satellite pass and in-situ measurements, sky
498 conditions and shallow water depth also likely introduced more errors at these locations. The R^2 between
499 R_{rs_OLCI} and R_{rs_insitu} at red and near infrared (NIR) bands was 0.89 when the data from station 3 and 4 were
500 excluded, suggesting good usability of these two bands for Chl a empirical algorithms in GB. Thus, the
501 higher the Chl a concentration, the stronger the red light absorption, resulting in higher reflectance at 709
502 nm; consequently, negative correlations were observed between Red/NIR band ratio and Chl a. The ratio
503 of Red (~673 nm) and NIR (709 nm) reflectance bands from in-situ measurements were overall highly
504 correlated with HPLC-measured Chl a with R^2 ~ 0.96, 0.94 and 0.98 on September 29, October 29 and
505 October 30, 2017, respectively (Fig. 9c). The Sentinel-3A OLCI Chl a maps (Fig. 10a-c) were generated
506 for all data based on the relationship between Chl a and the Red and NIR band ratio as:

507 $$\text{Chl a (μg L}^{-1}) = 216.38 \times \exp(-2.399 \times \frac{R_{rs}\,(673)}{R_{rs}\,(709)}) \quad \text{[All data]} \quad \ldots\ldots (16)$$
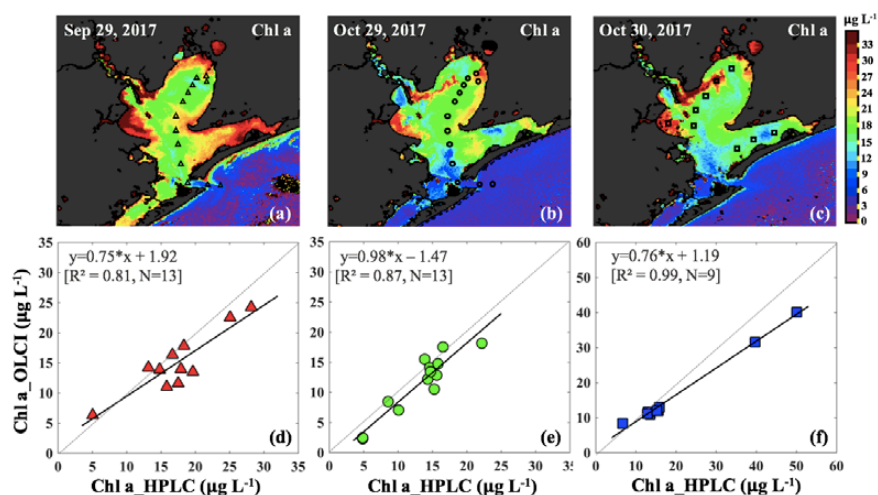
508

509 **Figure 10**. Chl a concentration generated based on in-situ band ratio ($R_{rs}673/R_{rs}709$) algorithm with (a),
510 (b) and (c) representing Chl a distribution on September 29, October 29 and October 30, 2017,
511 respectively; (c), (d) and (f) show the validation between HPLC-measured Chl a and OLCI-derived Chl a
512 on September 29, October 29 and October 30, 2017, respectively.

513 The OLCI-derived Chl a (Fig. 10a-c) showed a good spatial agreement with Chl a_HPLC (Fig. 10d-f). The
514 Chl a concentration on September 29, 2017 was overall higher than that on October 29-30, 2017 through
515 the entire bay. East Bay displayed very high Chl a concentration, with highest value (>30 µg L⁻¹)
516 observed on September 29, 2017 (Fig. 10a). The narrow shape and shallow topography of East Bay
517 results in relatively higher water residence time (Rayson et al. 2016); thus, the reduced exchange with
518 shelf waters likely lends the East Bay vulnerable to eutrophication. The average Chl a concentration on
519 October 29-30, 2017 were ~ 15 µg L⁻¹ along the transect (station 1-11) and ~4-6 µg/L (station 12-14)
520 close the entrance of GB. In addition, Chl a adjacent to San Jacinto River mouth (>16 µg L⁻¹) was higher
521 than that in Trinity Bay, which might suggest that San Jacinto inflow had higher nutrient concentrations
522 than Trinity as also previously reported (Quigg et al., 2010). Furthermore, the OLCI-Chl a maps on
523 October 29 and 30, 2017 showed extremely high Chl a in a narrow area adjacent to the San Jacinto River
524 mouth, with Chl a approaching ~ 40 µg L⁻¹ at station 19 (Fig. 10c).

525 ### 3.2.2   Reconstruction of Total Pigment Absorption Spectra from OLCI-derived Chl a

526 The reconstructed $a_{pig}(\lambda)$ based on the third order function of Chl a_HPLC (gray lines; Fig. 11a and b)
527 agreed well with the spectrophotometrically measured $a_{pig}(\lambda)$ (black lines; Fig. 11a and b) during both
528 surveys ($R^2=0.86$; Fig. 11c). The R^2 for modeled versus measured $a_{pig}(\lambda)$ are between 0.76 and 1.00 from
529 400 to 700 nm with averaged R^2 of whole spectra reaching ~ 0.82 on September 29, 2017 and ~0.89 on
530 October 29-30, 2017, respectively. The vector coefficients $C = [C_3, C_2, C_1, C_0]$ obtained from Eq. (11)
531 were further applied to Eq. (12) to generate $a_{pig\_OLCI}(\lambda)$ based on OLCI-derived Chl a images (Fig. 10a-c),
532 which contained 259×224 pixels in each image. The $a_{pig\_OLCI}(\lambda)$ at each pixel was retrieved at 1 nm
533 interval, and thus 301 images of $a_{pig\_OLCI}(\lambda)$ representing each wavelength were obtained over GB.

534
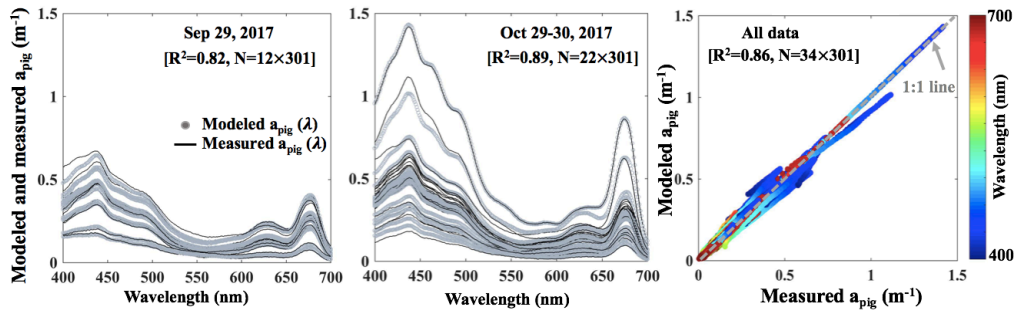
Figure 11. Spectrophotometrically measured and multi-regression fitted $a_{pig}(\lambda)$ spectra acquired on **(a)** September 29 and **(b)** October 29-30, 2017 in GB. Gray and black lines represent modeled and measured results, respectively. **(c)** Comparison between modeled and spectrophotometrically measured $a_{pig}(\lambda)$ for all data with color representing wavelength.

3.2.3   Accuracy of phytoplankton pigment retrievals from Sentinel 3A-OLCI

The reconstructed $a_{pig\_OLCI}(\lambda)$ was spectrally decomposed into 16 individual pigment spectra at each pixel based on Eq. (14). A comparison of HPLC-measured pigments to averaged NNLS inversion model retrieved pigments showed R^2 ranging from a low of 0.39 for violaxanthin to 0.98 for Chl a (Table 4). The NNLS-modeled Chl a also correlated well with OLCI-derived Chl a (R^2=0.98; Fig. 12a), with each exhibiting similar quantitative and spatial patterns. For the other 15 simultaneously simulated pigments, only 7 pigments averaged R^2 value greater than 0.65 (Table 4). Five NNLS-derived versus HPLC measured diagnostic pigments including alloxanthin, Chl b, zeaxanthin, fucoxanthin and peridinin are shown in Figure 12. The R^2 between NNLS-derived and HPLC-measured pigments for surveys 1 and 2 was highest for alloxanthin (0.91; Fig. 12b). For the other pigments R^2 was 0.78 for Chl b (Fig. 12c), 0.69 for zeaxanthin (Fig. 12d), 0.51 for fucoxanthin (Fig. 12e) and 0.50 for peridinin (Fig. 12f), respectively.

551
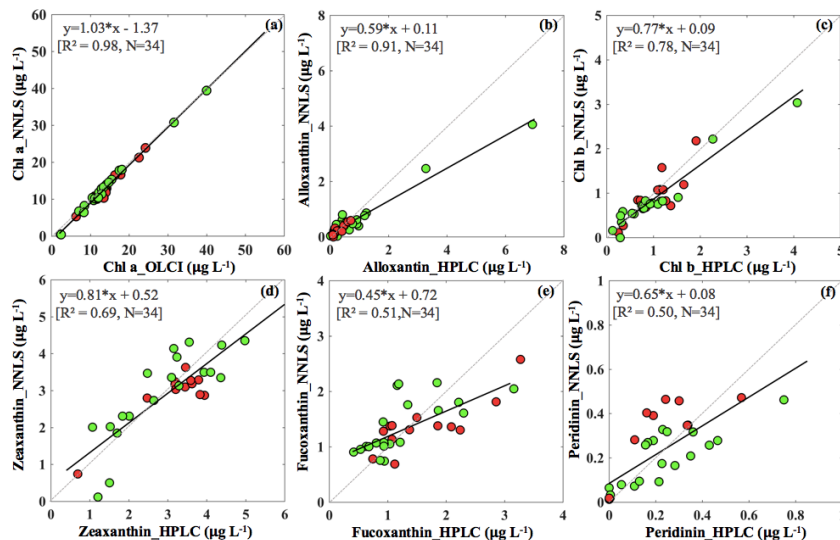
Figure 12. Sentinel-3A OLCI derived pigment concentration against HPLC measured pigment concentration in Galveston Bay; **a)** Chl a, **b)** alloxanthin, **c)** Chl-b, **d)** zeaxanthin, **e)** fucoxanthin, and **f)** peridinin.

Table 4. Correlation between HPLC-measured pigment concentration with NNLS-modeled pigments.

Pigments	Sep 29, 2017	Oct 29, 2017	Oct 30, 2017	Averaged R^2
Chl a	0.95	0.97	0.98	0.97
Chl b	0.76	0.77	0.95	0.82
Chl c_1	0.56	0.42	0.79	0.59
Chl c_2	0.49	0.45	0.74	0.56
Pheophythin a	0.76	0.79	0.72	0.75
Pheophythin b	0.75	0.88	0.76	0.79
Peridinin	0.65	0.48	0.51	0.54
Fucoxanthin	0.65	0.45	0.85	0.60
Neoxanthin	0.55	0.63	0.79	0.65
Lutein	0.61	0.78	0.72	0.70
Violaxanthin	0.43	0.34	0.39	0.39
Alloxanthin	0.81	0.40	0.91	0.72
Diadinoxanthin	0.69	0.40	0.89	0.66
Diatoxanthin	0.49	0.43	0.49	0.47
Zeaxanthin	0.76	0.65	0.78	0.73
β-carotenoid	0.41	0.42	0.82	0.55

3.3.1 Spatial Distributions of Diagnostic Pigments

Alloxanthin which is unique to cryptophytes (Wright and Jeffrey, 2006) exhibited spatial distributions patterns (Fig. 13a_1-c_1) that correlated reasonably well with Chl a distribution (Fig. 10a-c) during both surveys. Alloxanthin was especially low (~ 0.7 μg L^{-1}, Fig. 13a_1) in the major basin area on September 29, 2017. However, alloxanthin showed very high concentrations (~ 3.5 μg L^{-1}, Fig. 13a_1-c_1) adjacent to San Jacinto River mouth, which coincided with the high %Chl a of cryptophyte at stations 19 and 23 (Fig. 6b). The bloom with high concentration of alloxanthin on October 29, 2017 (~3.5 μg L^{-1}; Fig. 13b_1) then extended to a broader area on October 30, 2017 (Fig. 13c_1).

Chl b is abundant in the group of chlorophyte (green algae) (Hirata et al., 2011) and the spatial distributions of Chl b (Fig. 13a_2-c_2) as well showed strong correlations with Chl a (Fig. 10a-c) for both surveys. The NNLS-derived Chl b exhibited overall elevated concentrations throughout bay and were higher in northern part of the bay than the area adjacent to the nGOM. Chl b concentrations observed on September 29, 2017 were higher than that on October 29-30, 2017, which corresponded to a decline of chlorophyte percentage derived from the IOP inversion algorithm for survey 2 (Fig. 6). Furthermore, Chl b concentrations approached ~2.8 μg L^{-1} in the bloom area and the corresponding green discoloration of water was also observed during the field survey on October 30, 2017.

Zeaxanthin was considered as taxa-specific pigment for prokaryotes (cyanobacteria) (Moisan et al., 2017) and NNLS-derived zeaxanthin maps revealed higher concentrations during survey 2 compared to survey 1. Zeaxanthin distributions (Fig. 12a_3-c_3) displayed significantly different patterns than Chl a and exhibited relatively lower concentration in the mid-bay (around Smith Point) on September 29, 2017. Zeaxanthin also displayed especially low concentrations in the bloom area during survey 2; furthermore, low %Chl a of cyanobacteria was also observed at stations 19-24 (Fig. 6), thus indicating that this localized algal bloom event was not associated with cyanobacteria.

583 Fucoxanthin is a major carotenoid found in diatoms (Hirata et al., 2011; Moisan et al. 2017) and the
584 NNLS-derived fucoxanthin maps (Fig. 12a$_4$-c$_4$) showed highly similar distribution patterns with Chl a
585 maps on September 29, 2017, but distributions differed on October 29-30, 2017. More interestingly, maps
586 of fucoxanthin showed low concentrations around Smith Point on October 29-30, which also
587 corresponded to the relatively low %Chl a of diatom derived from IOP inversion algorithm at station 7, 8
588 and 9. In addition, relatively low concentration of fucoxanthin was observed in the bloom area for survey
589 2. Overall, fucoxanthin concentration in GB was relatively higher for survey 1, which corresponded to the
590 higher %Chl a of diatom (Fig. 6) compared to survey 2.
591
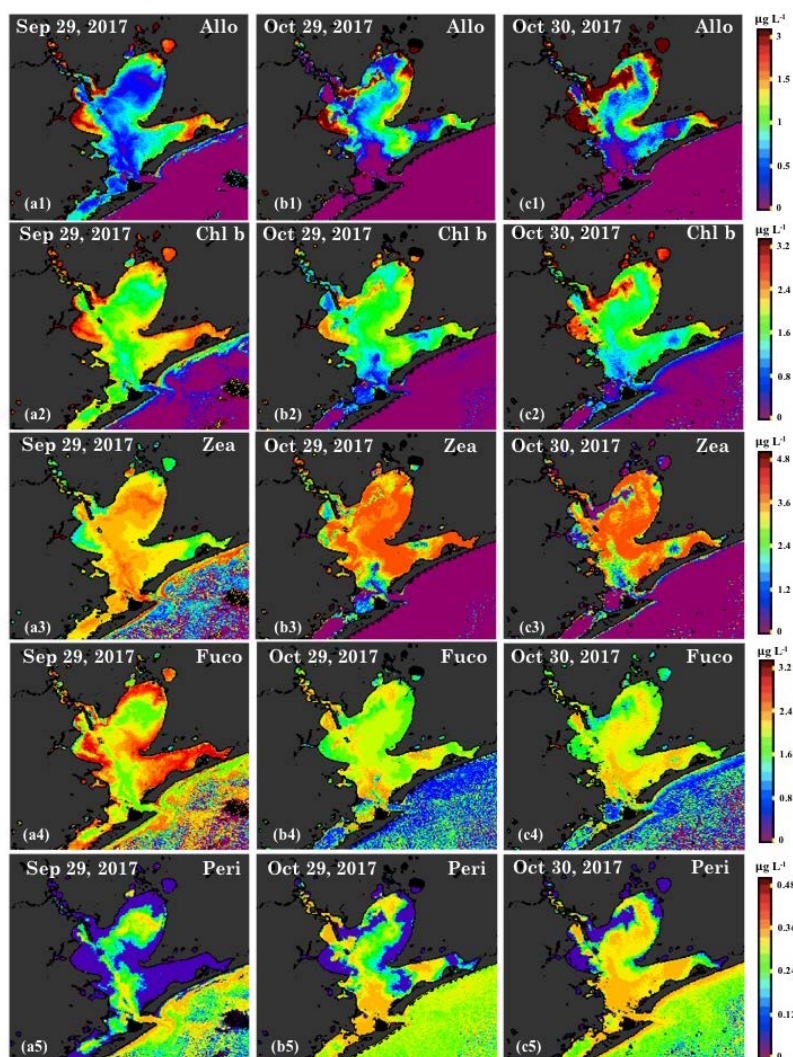
592
593 **Figure 13**. Sentinel-3 OLCI derived maps of diagnostic pigments for Galveston Bay. Simulated **a1-c1)**
594 alloxanthin, **a2-c2)** Chl b, **a3-c3)** zeaxanthin, **a4-c4)** fucoxanthin, and **a5-c5)** peridinin concentrations. a,
595 b and c represent columns (maps for 29 September, 29 and 30 October 2017) and 1-5 represent rows
596 (pigments), respectively.
597

Peridinin is a primary bio-marker pigment for certain dinoflagellates (Örnólfsdóttir et al., 2003). Peridinin concentrations were lowest in GB compared to other diagnostic pigments (0.001-0.05 µg L^{-1}), implying that dinoflagellate was not the dominant species during both surveys. Maps of peridinin (Fig. 12a$_5$-c$_5$) presented higher concentration (~0.3 µg L^{-1}) in higher salinity waters adjacent to the bay entrance, which agreed well with the increasing fraction of dinoflagellate at station 10-14 detected from IOP inversion model (Fig. 6). Furthermore, the areas with high concentrations of peridinin generally corresponded to lower Chl a concentrations during both surveys, this was especially obvious in the center of Trinity Bay and the entrance of GB on September 29, 2017, and bloom area on October 29-30, 2017. In addition, both fucoxanthin and peridinin pigments showed high concentrations along the Houston Ship Channel during survey 2.

4 Discussion

4.1 Performance of the Semi-Analytical IOP Inversion Algorithm

The residuals between R$_{rs\_insitu}$ and R$_{rs\_mod}$ on September 29 and October 29-30, 2017, are negative in the blue (400-450 nm) and red (610-630 nm) spectral range at most stations, whilst keeping positive ~700 nm, which could be attributed to a number of factors. First, the underestimation near 700 nm by the IOP inversion model is possibly induced by the absence of a fluorescence component in the IOP inversion model; thus, R$_{rs\_insitu}$ containing fluorescence signals were generally higher than R$_{rs\_mod}$ near 700 nm. Second, in the range of 610-630 nm, the absorption was overestimated at most of the stations; in this spectral range, the shape of spectra was strongly modulated by cyanobacteria absorption. Thus this overestimation ~620 nm is likely introduced by the input absorption spectrum (eigenvector) for cyanobacteria since all of input a$^*_{phi}$(λ) are general absorption spectral shapes for different phytoplankton groups. However, the spectra of a$^*_{phi}$(λ) can vary in magnitude and shape associated with package effects under different environmental conditions (e.g. nutrient, light and temperature) even for the same species (Bricaud et al., 2004). More detailed absorption spectra of phytoplankton under different conditions (e.g. high/low light and nutrient) could improve the performance of the IOP algorithm. Furthermore, the role of scattering might be another key factor to explain differences between R$_{rs\_insitu}$ and R$_{rs\_mod}$ for the whole spectra. The quantity and composition of suspended materials including phytoplankton, sediment and minerals will collaboratively determine b$_{bp}$(λ) in both shape and magnitude. However, the input eigenvector of b$_{bp}$(λ) in the present study was not divided into detailed sub-constituents and was a sum spectrum based on a power law function (Table 2). In reality, b$_{bp}$(λ) spectra are not smooth and regular, and thus, the b$_{bp}$(λ) value of phytoplankton and sediment might introduce errors to the whole spectrum due to their own scattering characteristics.

4.2 Distributions of NNLS-Retrieved Phytoplankton Pigments from Sentinel-3A OLCI

The derived maps of phytoplankton diagnostic pigments appeared to be reasonably correlated with HPLC-measured diagnostic pigments and showed overall agreement with extracted phytoplankton taxonomic compositions detected from the IOP inversion algorithm. The retrieved diatom-specific fucoxanthin maps however, showed high concentrations compared to other pigments adjacent to the entrance (Fig. 13b$_4$ and c$_4$), which contradicted with diatom %Chl a calculated from IOP inversion algorithm that Chl a fraction of diatom was relatively uniform at stations 12-14 (Fig. 6b). (Nair et al., 2008) concluded that fucoxanthin can occur in other phytoplankton types (e.g. raphidophyte and haptophyte). Fucoxanthin and/or fucoxanthin derivatives such as 19′-hexanoyloxyfucoxanthin can also replace peridinin as the major carotenoid in some dinoflagellates (e.g., *Karenia brevis*; Jeffrey and Vest, 1997). The elevated contributions from groups of dinoflagellate, haptophyte and prochlorophyte adjacent to the entrance (stations 10-14; Fig. 6b) along with high concentrations of fucoxanthin likely suggest the

643 presence of elevated fractions of haptophyte and dinoflagellate, and further implies that fucoxanthin is an
644 ambiguous marker pigment for diatoms. This could also explain the poor correlation between
645 inverted %Chl a and %DP observed for the groups of diatom and haptophyte (Fig. 4g and l). These results
646 also further suggest the inherent limitations of using DP-type comparison between major biomarker
647 pigments and phytoplankton groups because the major assumption for DP-type methods is that diagnostic
648 pigment of distinct phytoplankton groups are uncorrelated to each other. This assumption is invalid in that
649 concentrations of major biomarker pigments are significantly correlated with each other and also may
650 vary in time and space under some external environmental stress (e.g., temperature, salinity, mixing, light
651 and nutrient) (Latasa and Bidigare, 1998).

652 Chl a concentration is another crucial factor that influences the accuracy of retrieved pigments. The goal
653 of the empirical Chl a algorithm for Sentinel 3A-OLCI is to obtain more accurate estimation of surface
654 Chl a concentration, which is better for retrieving other accessory pigments. However, the primary
655 limitation of Chl a empirical algorithms in this study was that the derived relationships between Red/NIR
656 and Chl a in GB may only be valid within a specific time period due to temporally-limited field
657 observations versus highly dynamic estuarine environments. Therefore, a Chl a empirical algorithm that is
658 more broadly applicable over a longer time period will largely improve the accuracy of retrieved
659 pigments over a series of remote sensing images and can be more useful for spatiotemporal studies of
660 phytoplankton functional diversity. In addition, the similarity of many carotenoid absorption spectra
661 could as well introduce errors when applying spectral decomposition techniques. Thus, the 16 input
662 pigment spectra used in this study were selected from (Thrane et al., 2015), which were correctly
663 identified from unknown phytoplankton community structure with low error rate reported from Monte
664 Carlo tests to minimize the potential effects of aliasing the spectra.

665 **4.3 Response of Phytoplankton Taxonomic Composition to Environmental Conditions**

666 Previous studies showed phytoplankton community in GB to be primarily dominated by
667 diatoms/dinoflagellates during winter/spring, corresponding to the period of high fresh water discharge
668 and nutrient concentrations (Dorado et al., 2015), while, cyanobacteria were the dominant species during
669 the warmer months (Jun-Aug) (Roelke et al., 2013). However, perturbations following Hurricane Harvey
670 affected the phytoplankton taxonomic composition with alterations in phytoplankton community structure
671 were observed as GB system transitioned from marine to freshwater then to marine system. The decline
672 of Chl a during survey 2 likely resulted from the depletion of nutrients associated with floodwaters.
673 Higher fractions of diatom, cyanobacteria, and chlorophyte observed during survey 1 to some extent
674 agreed well with measurements of Steichen et al., 2018 two weeks following Hurricane Harvey wherein,
675 the phytoplankton community which was dominated by estuarine and marine diatoms and dinoflagellates
676 pre-Hurricane Harvey, then transitioned to primarily freshwater species (cyanobacteria and green algae)
677 immediately following the flooding event. The results of high cyanobacteria %Chl a accompanied by high
678 concentration of zeaxanthin further confirmed that cyanobacteria biomass could probably be enhanced by
679 high discharge of phosphorus-rich floodwaters (Schindler, 1977). In addition, the relatively higher
680 fraction of diatom observed during survey 1 in comparison to survey 2 was likely associated with the
681 rapid nutrient uptake rate of diatoms under high nutrient loading conditions after the freshwater inflows
682 (Örnólfsdóttir et al., 2004). The decline of diatoms and chlorophyte versus slightly increased
683 cyanobacteria observed during survey 2 could be due to the more rapid depletion of nutrients after the
684 flooding event. Some cyanobacteria species are nitrogen (N_2) fixers, which could succeed in low nitrogen
685 (N) waters (Howarth et al., 1988), and thus likely outcompeted diatoms and chlorophytes under more
686 seasonal conditions during survey 2. Further, the presence of green algae and cyanobacteria could as well
687 as be explained by the clarity and turbidity gradient of water. Quigg et al. (2010) reported that when
688 turbidity was relatively high, chlorophyte dominated over cyanobacteria with biomass ratio of
689 chlorophyte/cyanobacteria larger than 2, which supported our observations that chlorophyte dropped off

690   whilst cyanobacteria increased during survey 2. Highest cyanobacteria percentage in East Bay also
691   suggest that calm and stratified waters may accelerate cyanobacteria growth as the buoyancy regulation
692   mechanism of cyanobacteria is possibly restricted by water mixing. Dinoflagellates increased during
693   survey 2 and showed overall preference for high-salinity waters. Previous Imaging FlowCytobot (IFCB)
694   observations from Biological and Chemical Oceanography Data Management Office (BCO-DMO)
695   showed that algal blooms after hurricanes in the nGOM were initially dominated by diatoms, and
696   subsequently transitioned to blooms of dinoflagellates, likely associated with nutrient ratios and chemical
697   forms of nutrient supplied by the flood waters and rainfall. Generally, silica (Si) is essential for the
698   growth and reproduction of diatoms, whereas dinoflagellates show preference of higher phosphorus (P)
699   compared to some other groups (Heisler et al., 2008). In this study, distribution of fucoxanthin and
700   diatom %Chl a decreased from survey 1 to 2; in contrast, peridinin and dinoflagellate %Chl a showed
701   overall increased elevation during survey 2. Nutrient supply ratio with low N:P or Si:P could be a
702   contributor for shifting diatom-dominated community to dinoflagellates (Smayda et al., 1997). In addition,
703   high concentrations of fucoxanthin and peridinin observed along the Houston Ship Channel, which was
704   also shown in Steichen et al. (2018), might provide evidence that the ballast water addition from shipping
705   vessels likely promote harmful species of dinoflagellates and diatoms (Steichen et al., 2015).

706   The localized cryptophyte-chlorophyte bloom that occurred ~60d after Hurricane Harvey, was captured
707   by both satellite and in-situ measurements. This bloom might not be associated with the flooding events
708   of Hurricane Harvey, and could be linked to nutrient-rich runoff flowing into GB, reflecting sensitivity
709   and rapid response of phytoplankton community to nutrient input in GB. In shallow and turbid estuaries,
710   human activities are altering the environment and causing phytoplankton changes in diversity and
711   biomass to occur more frequently. Dugdale et al. (2012) reported that variations of phytoplankton
712   community in San Francisco estuary could be attributed to anthropogenically-elevated concentration of
713   ammonium, which restrain the uptake of nitrate, thus reducing the growth and reproduction of larger
714   diatoms and shifting towards smaller species (e.g., cryptophyte and green flagellate). Furthermore, 'pink
715   oyster' events related to alloxanthin of cryptophyte in GB occurred more frequently in recent years (Paerl
716   et al., 2003). The eastern side of Houston Ship Channel in mid bay region was reported as the area most
717   heavily impacted by the intense 'pink oyster' events. Previous studies and present observations both
718   suggest that this cryptophyte-chlorophyte dominated bloom could be promoted by the nutrient-driven
719   eutrophication from Houston Ship Channel, urbanization and industrialization along the upper San Jacinto
720   River complex.

721   **4.4 Photo-Physiological State of Natural Phytoplankton Community**

722   In this study, the CDOM-corrected F_V/F_M and σ_{PSII} likely represented a composite of both phytoplankton
723   taxonomy and physiological stress (e.g., nutrient and mixing). Typically, lowest N and P concentrations
724   were measured closest to the nGOM (Quigg et al., 2009). Phytoplankton community living close to
725   nGOM were usually in poor nutrient conditions and would be expected to maximize their light harvesting
726   (increase in σ_{PSII}) due to nutrient stress. Simultaneously, phytoplankton cells might experience a decline
727   of functional proportion of reaction centers of PSII (RCII), which means decrease in F_V/F_M. The observed
728   low levels of F_V/F_M and Chl a/TP versus high values of σ_{PSII} and AP/TP adjacent to the nGOM showed
729   agreement with previous studies that the fraction of carotenoids to be higher for nutrient-poor cultures
730   (Schitüter et al., 1997; Holmboe et al., 1999). In contrast, phytoplankton in well-mixed waters (station 7-9)
731   might experience abundant nutrients due to the resuspension associated with the cyclonic gyre around
732   Smith Points; as such, their photosynthetic machinery were likely healthier. Aiken et al. (2004)
733   documented that the Chl a/TP ratio was relatively higher when plants were in good growing conditions,
734   which is similar to the observations in this study that phytoplankton have higher fraction of Chl a
735   accompanying higher rate of photosynthetic efficiency (F_V/F_M) under nutrient replete conditions. Overall,
736   the spatial pattern of F_V/F_M and σ_{PSII} in GB could be mainly attributed to physiological stress of nutrient

737   and hydrodynamics conditions since the light availability (PAR) during the sampling period did not vary
738   much spatially at the surface. Furthermore, FIRe measurements (F_V/F_M and σ_{PSII}) also presented a
739   taxonomic signal super-imposed upon environmental factors. Each cluster with different dominant taxa
740   (well mixed group, chlorophyte & cryptophyte, cyanobacteria, and dinoflagellate & haptophyte)
741   displayed different physiological characteristics. The taxonomic sequence of eukaryotic groups from high
742   F_V/F_M, low σ_{PSII} to low F_v/F_M, high σ_{PSII} in the present observations showed potential effects of
743   phytoplankton cell size corresponding to diatoms, chlorophyte, and cryptophyte, dinoflagellate and
744   haptophyte. The prokaryote (cyanobacteria) had relatively high values of F_V/F_m and low values of σ_{PSII};
745   this agreed with F_V/F_M for some species of nitrogen-fixing cyanobacteria that can range from 0.6 to 0.65
746   (Berman-Frank et al., 2007). Yet, it is difficult to separate the contributions from environmental factors
747   and taxonomic variations to the changes of FIRe fluorescence signals since all these parameters are inter-
748   related. Different phytoplankton groups/sizes will display distinct physiological traits (F_V/F_M and σ_{PSII})
749   when experiencing considerable environmental pressures. Thus, effects of physiological stress on
750   F_V/F_M and σ_{PSII} variations for natural samples can only be determined when taxonomic composition can
751   be excluded as a contributor (Suggett et al., 2009).

752   ## 5 Conclusions

753   Field measurements (salinity, pigments, optical properties and physiological parameters) and ocean color
754   observations from Sentinel-3A OLCI were used to study the effects of extreme flooding associated with
755   Hurricane Harvey on the phytoplankton community structures, pigment distributions and their
756   physiological state in GB. Flooding effects made the entire GB transition from saline to freshwater then
757   back to a more marine influenced system. The band ratio (Red/NIR) of R_{rs_insitu} were negatively correlated
758   with HPLC-measured Chl a in an exponential relationship ($R^2 > 0.93$). The satellite-retrieved Chl a maps
759   yielded much higher Chl a concentration on September 29, 2017 compared to October 29-30, 2017 with
760   lowest Chl a observed adjacent to the shelf waters. Phytoplankton taxonomic composition was further
761   retrieved from R_{rs_insitu} using a 10-species IOP inversion algorithm. Phytoplankton community generally
762   dominated by estuarine marine diatoms/dinoflagellates before flood events, was altered to freshwater
763   species of green algae (chlorophyte) and cyanobacteria during survey 1. It also showed an increase of
764   small-size species including cryptophyte, haptophyte, prochlorophyte and cyanobacteria accompanied by
765   a decline of chlorophyte and diatoms during survey 2.

766   Phytoplankton diagnostic pigments which were retrieved using an NNLS inversion model based on
767   Sentinel-3A OLCI Chl a maps also confirmed spatiotemporal variations of phytoplankton taxonomy. The
768   NNLS-retrieved diagnostic pigment maps showed overall spatiotemporal agreement with HPLC
769   measurements with R^2 ranging from 0.39 (violaxanthin) to 0.98 (Chl a). Chl b showed overall higher
770   concentrations during survey 1 compared to survey 2, and its distribution displayed highly similar
771   patterns with Chl a. Alloxanthin showed especially low concentration in the main basin area but very high
772   concentration in a localized bloom area adjacent to the San Jacinto River mouth. Zeaxanthin presented
773   significantly different patterns with other pigments during both the surveys. Concentration of peridinin
774   was overall low inside of GB, and generally displayed high concentrations in areas where Chl a was low.

775   Finally, the retrieved phytoplankton taxonomic compositions from the IOP inversion algorithm were
776   linked with FIRe-measured photosynthetic parameters (F_V/F_M and σ_{PSII}) to assess the effects of
777   physiological stress and taxonomic contributions on phytoplankton photosynthetic performance. An
778   inverse relationship between the F_V/F_M and σ_{PSII} were observed during both surveys. Phytoplankton
779   community in well-mixed waters (around Smith Point) showed high F_V/F_M against low σ_{PSII}; in contrast,
780   the area with poor nutrient conditions (adjacent to the shelf waters), showed low F_V/F_M and elevated
781   σ_{PSII}. Taxonomic signatures of F_v/F_m and σ_{PSII} revealed diverse physiological characteristics with
782   dinoflagellate-haptophyte group showing the lowest F_V/F_M versus the highest σ_{PSII}, whereas prokaryote

783 of cyanobacteria-dominated group showed high values of F_V/F_M and low values of σ_{PSII}. Overall, this
784 study using field and ocean color data combined with inversion algorithms provided novel insights on
785 phytoplankton response to an extreme flood perturbation in a turbid estuarine environment based on
786 taxonomy, pigment composition and physiological state of phytoplankton.

787

788 *Data availability.* Data from field measurements are available upon request from the corresponding
789 author.
790
791 *Author contributions.* BL and ED conceived and designed the research; BL, ED and IJ collected and
792 processed the data; BL analyzed the data and all authors contributed to writing the paper.
793
794 *Competing interests.* The authors declare that they have no conflict of interest.

795 *Acknowledgements.* The authors thank the European Space Agency (ESA) and the European Organization
796 for Meteorological Satellites (EUMESAT) for providing access to the Sentinel-3 OLCI ocean color data
797 and the Sentinel-3 Toolbox Kit Module (S3TBX) version 5.0.1 in Sentinel Application Platform (SNAP).
798 We are also grateful to Bill Gibson from the Coastal Studies Institute for providing logistic support for
799 field operations. EJD acknowledges NASA support through grant No. 80NSSC18K0177.

800

801 **References**

802 Acker, J., Lyon, P., Hoge, F., Shen, S., Roffer, M., and Gawlikowski, G.: Interaction of Hurricane Katrina with
803 optically complex water in the Gulf of Mexico: interpretation using satellite-derived inherent optical properties
804 and chlorophyll concentration, IEEE Geosci. and Remote Sens. Lett., 6, 209-213, 2009.
805 Aiken, J., Fishwick, J., Moore, G., and Pemberton, K.: The annual cycle of phytoplankton photosynthetic
806 quantum efficiency, pigment composition and optical properties in the western English Channel, J. Mar. Biol.
807 Assoc. U. K., 84, 301-313, 2004.
808 Alvain, S., Moulin, C., Dandonneau, Y., and Bréon, F.-M.: Remote sensing of phytoplankton groups in case 1
809 waters from global SeaWiFS imagery, Deep Sea Res., Part I, 52, 1989-2004, 2005.
810 Barlow, R., Cummings, D., and Gibb, S.: Improved resolution of mono-and divinyl chlorophylls a and b and
811 zeaxanthin and lutein in phytoplankton extracts using reverse phase C-8 HPLC, Mar. Ecol. Progr. Ser., 161,
812 303-307, 1997.
813 Behrenfeld, M. J., and Falkowski, P. G.: Photosynthetic rates derived from satellite-based chlorophyll
814 concentration, Limnol. Oceanogr., 42, 1-20, 1997.
815 Behrenfeld, M. J., and Kolber, Z. S.: Widespread iron limitation of phytoplankton in the South Pacific Ocean,
816 Science, 283, 840-843, 1999.
817 Berman-Frank, I., Quigg, A., Finkel, Z. V., Irwin, A. J., and Haramaty, L.: Nitrogen-fixation strategies and Fe
818 requirements in cyanobacteria, Limnol. Oceanogr., 52, 2260-2269, 2007.
819 Bidigare, R. R., Ondrusek, M. E., Morrow, J. H., and Kiefer, D. A.: In-vivo absorption properties of algal
820 pigments, Ocean Optics X, Intl. Soc. Opt. Photonics., 1302, 290-303, 1990.
821 Blondeau-Patissier, D., Gower, J. F., Dekker, A. G., Phinn, S. R., and Brando, V. E.: A review of ocean color
822 remote sensing methods and statistical techniques for the detection, mapping and analysis of phytoplankton blooms
823 in coastal and open oceans, Progr. Oceanogr., 123, 123-144, 2014.
824 Bracher, A., Taylor, M., Taylor, B., Dinter, T., Roettgers, R., and Steinmetz, F.: Using empirical orthogonal
825 functions derived from remote sensing reflectance for the prediction of phytoplankton pigments concentrations,
826 Ocean Sci., 11, 139-158, 2015.

827   Brewin, R. J., Sathyendranath, S., Hirata, T., Lavender, S. J., Barciela, R. M., and Hardman-Mountford, N. J.: A
828   three-component model of phytoplankton size class for the Atlantic Ocean, Ecol. Modell., 221, 1472-1483, 2010.
829   Bricaud, A., Claustre, H., Ras, J., and Oubelkheir, K.: Natural variability of phytoplanktonic absorption in oceanic
830   waters: Influence of the size structure of algal populations, J. Geophys. Res. Oceans, 109, C11010–1, 2004.
831   Campbell, D., Hurry, V., Clarke, A. K., Gustafsson, P., and. Öquist, G.: Chlorophyll fluorescence analysis of
832   cyanobacterial photosynthesis and acclimation, Microbiol. Molecul. Biol. Rev., 62, 667-683, 1988.
833   Carder, K. L., Chen, F., Lee, Z., Hawes, S., and Kamykowski, D.: Semianalytic Moderate-Resolution Imaging
834   Spectrometer algorithms for chlorophyll a and absorption with bio‐optical domains based on nitrate‐depletion
835   temperatures, J. Geophys. Res. Oceans, 104, 5403-5421, 1999.
836   Chase, A., Boss, E., Zaneveld, R., Bricaud, A., Claustre, H., Ras, J., Dall'Olmo, G., and Westberry, T. K.:
837   Decomposition of in situ particulate absorption spectra, Meth. Oceanogr., 7, 110-124, 2013.
838   Chase, A., Boss, E., Cetinić, I., and Slade, W.: Estimation of phytoplankton accessory pigments from hyperspectral
839   reflectance spectra: toward a global algorithm, J. Geophys. Res. Oceans, 122, 9725-9743, 2017.
840   Ciotti, A. M., Lewis, M. R., and Cullen, J. J.: Assessment of the relationships between dominant cell size in natural
841   phytoplankton communities and the spectral shape of the absorption coefficient, Limnol. Oceanogr., 47, 404-417,
842   2002.
843   Cullen, J. J., and Davis, R. F.: The blank can make a big difference in oceanographic measurements, Limnol.
844   Oceanogr., 12, 29-35, 2003.
845   D'Sa, E. J., Lohrenz, S. E., Asper, V. L., and Walters, R. A.: Time series measurements of chlorophyll fluorescence
846   in the oceanic bottom boundary layer with a multisensor fiber-optic fluorometer, J. Atmos. Ocean. Technol., 14,
847   889-896, 1997.
848   D'Sa, E. J., and Lohrenz, S. E.: Theoretical treatment of fluorescence detection by a dual-fiber-optic sensor with
849   consideration of sampling variability and package effects associated with particles, Appl. Optics, 38, 2524-2535,
850   1999.
851   D'Sa, E. J., Miller, R. L., and Del Castillo, C.: Bio-optical properties and ocean color algorithms for coastal waters
852   influenced by the Mississippi River during a cold front, Appl. Optics, 45, 7410-7428, 2006.
853   D'Sa, E. J., Korobkin, M., and Ko, D. S.: Effects of Hurricane Ike on the Louisiana–Texas coast from satellite and
854   model data, Remote Sens. Lett., 2, 11-19, 2011.
855   D'Sa, E. J.: Assessment of chlorophyll variability along the Louisiana coast using multi-satellite data, GISci. Remote
856   Sens., 51, 139-157, 2014.
857   D'Sa, E. J., Joshi, I., and Liu, B.: Galveston Bay and coastal ocean optical geochemical response to Hurricane
858   Harvey from VIIRS ocean color, Geophys. Res. Lett., 45, 10579-10589, https://doi.org/10.1029/2018GL079954,
859   2018.
860   Devred, E., Sathyendranath, S., Stuart, V., and Platt, T.: A three component classification of phytoplankton
861   absorption spectra: Application to ocean-color data, Remote Sens. Environ., 115, 2255-2266, 2011.
862   Dierssen, H. M., Kudela, R. M., Ryan, J. P., and Zimmerman, R. C.: Red and black tides: Quantitative analysis of
863   water-leaving radiance and perceived color for phytoplankton, colored dissolved organic matter, and suspended
864   sediments, Limnol. Oceanogr., 51, 2646-2659, 2006.
865   Doerffer, R., and Schiller, H.: The MERIS Case 2 water algorithm, Intl. J. Remote Sens., 28, 517-535, 2007.
866   Dorado, S., Booe, T., Steichen, J., McInnes, A. S., Windham, R., Shepard, A., Lucchese, A. E., Preischel, H.,
867   Pinckney, J. L., and Davis, S. E.: Towards an understanding of the interactions between freshwater inflows and
868   phytoplankton communities in a subtropical estuary in the Gulf of Mexico, PLoS One, 10, e0130931, 2015.
869   Dugdale, R., Wilkerson, F., Parker, A. E., Marchi, A., and Taberski, K.: River flow and ammonium discharge
870   determine spring phytoplankton blooms in an urbanized estuary, Estuar. Coast. Shelf Sci., 115, 187-199, 2012.
871   Dutkiewicz, S., Hickman, A. E., Jahn, O., Gregg, W. W., Mouw, C. B., and Follows, M. J.: Capturing optically
872   important constituents and properties in a marine biogeochemical and ecosystem model, Biogeosciences, 12, 4447-
873   4481, 2015.
874   Farfan, L. M., D'Sa, E. J., and Liu, K.: Tropical cyclone impacts on coastal regions: the case of the Yucatan and the
875   Baja California Peninsulas. Mexico, Estuar. Coast., 37, 1388-1402, 2014.
876   Ficek, D., Kaczmarek, S. a., Stoñ-Egiert, J., Wozniak, B., Majchrowski, R., and Dera, J.: Spectra of light absorption
877   by phytoplankton pigments in the Baltic; conclusions to be drawn from a Gaussian analysis of empirical data,
878   Oceanologia, 46, 533-555, 2004.

Fishwick, J. R., Aiken, J., Barlow, R., Sessions, H., Bernard, S., and Ras, J.: Functional relationships and bio-optical properties derived from phytoplankton pigments, optical and photosynthetic parameters; a case study of the Benguela ecosystem, J. Mar. Biol. Assoc. U. K., 86, 1267-1280, 2006.

Garver, S. A., and Siegel, D. A.: Inherent optical property inversion of ocean color spectra and its biogeochemical interpretation: 1. Time series from the Sargasso Sea, J. Geophys. Res., Oceans, 102, 18607-18625, 1997.

Geider, R. J., La Roche, J., Greene, R. M., and Olaizola, M.: Response of the photosynthetic apparatus of phaeodactylum tricornutum (bacillariophyceae to nitrate, phosphate, or iron starvation, J. Phycol., 29, 755-766, 1993.

Gitelson, A.: The peak near 700 nm on radiance spectra of algae and water: relationships of its magnitude and position with chlorophyll concentration, Int. J. Remote Sens., 13, 3367-3373, 1992.

Gordon, H. R., Brown, O. B., Evans, R. H., Brown, J. W., Smith, R. C., Baker, K. S., and Clark, D. K.: A semianalytic radiance model of ocean color, J. Geophys. Res., Atmos., 93, 10909-10924, 1988.

Guthrie, C. G., Matsumoto, J., and Solis, R.: Analysis of the influence of water plan strategies on inflows and salinity in Galveston Bay, Final report to the United States Army Corps of Engineers, Contract #R0100010015. Texas Water Development Board, Austin, Texas, USA, 71 pp., 2012.

Heisler, J., Glibert, P. M., Burkholder, J. M., Anderson, D. M., Cochlan, W., Dennison, W. C., and Lewitus, A.: Eutrophication and harmful algal blooms: a scientific consensus, Harmful Algae, 8, 3-13, 2008.

Hirata, T., Aiken, J., Hardman-Mountford, N., Smyth, T. J., and. Barlow, R. G.: An absorption model to determine phytoplankton size classes from satellite ocean colour, Remote Sens. Environ., 112, 3153–3159, 2008.

Hirata, T., Hardman-Mountford, N., Brewin, R., Aiken, J., Barlow, R., Suzuki, K., Isada, T., Howell, E., Hashioka, T., Noguchi-Aita, M., and Yamanaka, Y.: Synoptic relationships between surface Chlorophyll-a and diagnostic pigments specific to phytoplankton functional types. Biogeosciences, 8, 311–327, 2011.

Hoepffner, N., and Sathyendranath, S.: Effect of pigment composition on absorption properties of phytoplankton, Mar. Ecol. Progr. Ser., 73, l-23, 1991.

Hoge, F. E., and Lyon, P. E.: Satellite retrieval of inherent optical properties by linear matrix inversion of oceanic radiance models: an analysis of model and radiance measurement errors, J. Geophys. Res., Oceans, 101, 16631-16648, 1996.

Holmboe, N., Jensen, H. S., and Andersen, F. Ø.: Nutrient addition bioassays as indicators of nutrient limitation of phytoplankton in a eutrophic estuary, Mar. Ecol. Progr. Ser., 186, 95-104, 1999.

Howarth, R. W., Marino, R., Lane, J., and Cole, J. J.: Nitrogen fixation in freshwater, estuarine, and marine ecosystems. 1. Rates and importance, Limnol. Oceanogr., 33, 669-687, 1988.

Hu, C., Cannizzaro, J., Carder, K. L., Muller-Karger, F. E., and Hardy, R.: Remote detection of Trichodesmium blooms in optically complex coastal waters: Examples with MODIS full-spectral data, Remote Sens. Environ., 114, 2048-2058, 2010.

Hu, C., and Feng, L.: Modified MODIS fluorescence line height data product to improve image interpretation for red tide monitoring in the eastern Gulf of Mexico, J. Appl. Remote Sens., 11, 012003, 2016.

Jeffrey, S., and Vest, M.: Introduction to marine phytoplankton and their pigment signatures, in: Phytoplankton pigment in oceanography, edited by: Jeffrey, S.W., Mantoura, R. F. C., and Wright, S. W., UNESCO Publishing, Paris, France, 37-84, 1997.

Joshi, I. D., and D'Sa, E. J.: Seasonal variation of colored dissolved organic matter in Barataria Bay, Louisiana, using combined Landsat and field data, Remote Sens., 7, 12478-12502, 2015.

Joshi, I. D., D'Sa, E. J., Osburn, C. L., Bianchi, T. S., Ko, D. S., Oviedo-Vargas, D., Arellano, A. R., and Ward, N. D.: Assessing chromophoric dissolved organic matter (CDOM) distribution, stocks, and fluxes in Apalachicola Bay using combined field, VIIRS ocean color, and model observations, Remote Sens. Environ., 191, 359-372, 2017.

Joshi, I. D., and D'Sa, E. J.: An estuarine tuned Quasi-Analytical Algorithm for VIIRS (QAA-V): assessment and application to satellite estimates of SPM in Galveston Bay following Hurricane Harvey. Biogeosciences, 15, 4065-4086, 2018.

Kolber, Z. S., Zehr, J., and Falkowski, P. G.: Effects of growth irradiance and nitrogen limitation on photosynthetic energy conversion in photosystem II, Plant Physiol., 88, 923-929, 1988.

Kolber, Z. S., Prášil, O., and Falkowski, P. G.: Measurements of variable chlorophyll fluorescence using fast repetition rate techniques: defining methodology and experimental protocols, Biochim. Biophys. Acta (BBA)-Bioenergetics, 1367, 88-106, 1998.

Latasa, M., and Bidigare, R. R.: A comparison of phytoplankton populations of the Arabian Sea during the Spring Intermonsoon and Southwest Monsoon of 1995 as described by HPLC-analyzed pigments, Deep Sea Res., Part II, 45, 2133-2170, 1998.

Lee, Z., Carder, K. L., Peacock, T., Davis, C., and Mueller, J.: Method to derive ocean absorption coefficients from remote-sensing reflectance, Appl. Optics, 35, 453-462, 1996.

935 Lee, Z., Carder, K. L., and Arnone, R. A.: Deriving inherent optical properties from water color: a multiband quasi-
936 analytical algorithm for optically deep waters, Appl. Optics, 41, 5755-5772, 2002.
937 Lohrenz, S. E., Weidemann, A. D., and Tuel, M.: Phytoplankton spectral absorption as influenced by community
938 size structure and pigment composition J. Plankton Res., 25, 35-61, 2003.
939 Lutz, V. A., Sathyendaranath, S., Head, E. J., and Li, W. K.: Changes in the in vivo absorption and fluorescence
940 excitation spectra with growth irradiance in three species of phytoplankton, J. Plankton Res., 23, 555-569, 2001.
941 Mackey, M., Mackey, D., Higgins, H., and Wright, S.: CHEMTAX-a program for estimating class abundances from
942 chemical markers: application to HPLC measurements of phytoplankton, Mar. Ecol. Progr. Ser., 144, 265-283, 1996.
943 Maritorena, S., Siegel, D. A., and Peterson, A. R.: Optimization of a semianalytical ocean color model for global-
944 scale applications, Appl. Optics, 41, 2705-2714, 2002.
945 Moisan, T. A., Moisan, J. R., Linkswiler, M. A., and Steinhardt, R. A.: Algorithm development for predicting
946 biodiversity based on phytoplankton absorption, Cont. Shelf Res., 55, 17-28, 2013.
947 Moisan, T. A., Rufty, K. M., Moisan, J. R., and Linkswiler, M. A.: Satellite observations of phytoplankton
948 functional type spatial distributions, phenology, diversity, and ecotones, Front. Mar. Sci., 4, 189, 2017.
949 Moore, C. M., Suggett, D. J., Holligan, P. M., Sharples, J., Abraham, E. R., Lucas, M. I., Rippeth, T. P., Fisher, N.
950 R., Simpson, J. H., and Hydes, D. J.: Physical controls on phytoplankton physiology and production at a shelf sea
951 front: a fast repetition-rate fluorometer based field study, Mar. Ecol. Progr. Ser., 259, 29-45, 2003.
952 Moore, C. M., Suggett, D. J., Hickman, A. E., Kim, Y.-N., Tweddle, J. F., Sharples, J., Geider, R. J., and Holligan, P.
953 M.: Phytoplankton photoacclimation and photoadaptation in response to environmental gradients in a shelf sea,
954 Limnology and Oceanography, 51, 936-949, 2006.
955 Morel, A., and Prieur, L.: Analysis of variations in ocean color 1, Limnol. Oceanogr., 22, 709-722, 1977.
956 Nair, A., Sathyendranath, S., Platt, T., Morales, J., Stuart, V., Forget, M.-H., Devred, E., and Bouman, H.: Remote
957 sensing of phytoplankton functional types, Remote Sens. Environ., 112, 3366-3375, 2008.
958 Naik, P., D'Sa, E. J., Gomes, H. R., Goes, J. I., and Mouw, C. B.: Light absorption properties of southeastern Bering
959 Sea waters: Analysis, parameterization and implications for remote sensing, Remote Sens. Environ., 134, 120-134,
960 2013.
961 Örnólfsdóttir, E. B., Pinckney, J. L., and Tester, P. A.: Quantification of the relative abundance of the toxic
962 dinoflagellate, karenia brevis (dinophyta), using unique photopigments, J. Phycol., 39, 449-457, 2003.
963 Örnólfsdóttir, E. B., Lumsden, S. E., and Pinckney, J. L.: Nutrient pulsing as a regulator of phytoplankton
964 abundance and community composition in Galveston Bay, Texas, J. Experiment. Mar. Biol. Ecol., 303, 197-220,
965 2004.
966 Paerl, H. W., Valdes, L. M., Pinckney, J. L., Piehler, M. F., Dyble, J., and Moisander, P. H.: Phytoplankton
967 photopigments as indicators of estuarine and coastal eutrophication, AIBS Bull., 53, 953-964, 2003.
968 Pan, X., Mannino, A., Russ, M. E., Hooker, S. B., and Harding Jr, L. W.: Remote sensing of phytoplankton pigment
969 distribution in the United States northeast coast, Remote Sens. Environ., 114, 2403-2416, 2010.
970 Pan, X., Mannino, A., Marshall, H. G., Filippino, K. C., and Mulholland, M. R.: Remote sensing of phytoplankton
971 community composition along the northeast coast of the United States, Remote Sens. Environ., 115, 3731-3747,
972 2011.
973 Quigg, A., Roelke, D., and Davis, S. E.: Freshwater inflows and the health of Galveston Bay: influence of nutrient
974 and sediment load on the base of the food web, Final report of the coastal coordination council pursuant to National
975 Oceanic and Atmospheric Administration Award No. NA07NOS4190144, Texas A&M University at Galveston,
976 Texas, USA, 49 pp., 2009.
977 Quigg, A., Litherland, S., Phillips, J., and Kevekordes, K.: Phytoplankton productivity across Moreton Bay,
978 Queensland, Australia: the impact of water quality, light and nutrients on spatial patterns, in: Proceedings of the 13th
979 International Marine Biological Workshop, Moreton Bay, Queensland, Australia, 7-25 February, 2005, 355-372,
980 2010.
981 Quigg, A. S.: Understanding the role of nutrients in defining phytoplankton responses in the Trinity-San Jacinto
982 Estuary, Final report to Interagency Cooperative Contract No. 1104831134, Texas A & M University at Galveston,
983 Texas, USA, 56 pp., 2011.
984 Rayson, M. D., Gross, E. S., Hetland, R. D., and Fringer, O. B.: Time scales in Galveston Bay: An unsteady estuary,
985 J. Geophys. Res., Oceans, 121, 2268–2285, 2016.
986 Ritchie, R. J.: Consistent sets of spectrophotometric chlorophyll equations for acetone, methanol and ethanol
987 solvents, Photosynthesis Res., 89, 27-41, 2006.
988 Roelke, D. L., Li, H.-P., Hayden, N. J., Miller, C. J., Davis, S. E., Quigg, A., and Buyukates, Y.: Co-occurring and
989 opposing freshwater inflow effects on phytoplankton biomass, productivity and community composition of
990 Galveston Bay, USA, Mar. Ecol. Progr. Ser., 477, 61-76, 2013.

991 Roesler, C. S., and Perry, M. J.: In situ phytoplankton absorption, fluorescence emission, and particulate
992 backscattering spectra determined from reflectance, *J. Geophys. Res., Oceans*, 100, 13279-13294, 1995.
993 Roesler, C. S., and Boss, E.: Spectral beam attenuation coefficient retrieved from ocean color inversion, Geophys.
994 Res. Lett., 30, 2003.
995 Roesler, C. S., Etheridge, S. M., and Pitcher, G. C.: Application of an ocean color algal taxa detection model to red
996 tides in the Southern Benguela, in: Proceedings of the Xth International Conference on Harmful Algae, Florida Fish
997 and Wildlife Conservation Commission and Intergovernmental Oceanographic Commission of UNESCO, St.
998 Petersburg, Florida, USA, October, 2002, 303-305, 2003.
999 Sathyendranath, S., Aiken, J., Alvain, S., Barlow, R., Bouman, H., Bracher, A., Brewin, R., Bricaud, A., Brown, C.,
1000 and Ciotti, A.: Phytoplankton functional types from Space, in: (Reports of the International Ocean-Colour
1001 Coordinating Group (IOCCG); 15), International Ocean-Colour Coordinating Group, 1-156, 2014.
1002 Schindler, D. W.: Evolution of phosphorus limitation in lakes, Science, 196, 260–262, 1977.
1003 Schitüter, L., Riemann, B., and Søndergaard, M.: Nutrient limitation in relation to phytoplankton
1004 carotenoid/chiorophyll a ratios in freshwater mesocosms, J. Plankton Res., 19, 891-906, 1997.
1005 Smayda, T. J.: Harmful algal blooms: their ecophysiology and general relevance to phytoplankton blooms in the sea,
1006 Limnol. Oceanogr., 42, 1137–1153, 1997.
1007 Steichen, J. L., Denby, A., Windham, R., Brinkmeyer, R., and Quigg, A.: A tale of two ports: Dinoflagellate and
1008 diatom communities found in the high ship traffic region of Galveston Bay, Texas (USA), J. Coastal Res., 31(2),
1009 407-416, 2015.
1010 Steichen, J. L., Windham, R., Hala, D., Kaiser, K., Labonte, J. M., Petersen, L. H., Bacosa, H., Bretherton, L.,
1011 Kamalanathan, M., Setta, S., and Quigg, A.: Rapid physicochemical and biological assessment of Galveston Bay in
1012 the wake of Hurricane Harvey, abstract#AI44D-3023, in: Ocean Sciences Meeting 2018, American Geophysical
1013 Union, Portland, Oregon, USA, February, 2018.
1014 Stramski, D., Reynolds, R. A., Kaczmarek, S., Uitz, J., and Zheng, G.: Correction of pathlength amplification in the
1015 filter-pad technique for measurements of particulate absorption coefficient in the visible spectral region, Appl.
1016 Optics, 54, 6763-6782, 2015.
1017 Suggett, D. J., Warner, M. E., Smith, D. J., Davey, P., Hennige, S., and Baker, N. R.: Photosynthesis and production
1018 of hydrogen peroxide by Symbiodinium (pyrrhophyta) phylotypes with different thermal tolerances 1, J. Phycol, 44,
1019 948-956, 2008.
1020 Suggett, D. J., Moore, C. M., Hickman, A. E., and Geider, R. J.: Interpretation of fast repetition rate (FRR)
1021 fluorescence: signatures of phytoplankton community structure versus physiological state, Mar. Ecol. Progr. Ser.,
1022 376, 1-19, 2009.
1023 Sun, D., Huan, Y., Qiu, Z., Hu, C., Wang, S., and He, Y.: Remote-sensing estimation of phytoplankton size classes
1024 from GOCI satellite measurements in Bohai Sea and Yellow Sea, J. Geophys. Res. Oceans, 122, 8309-8325, 2017.
1025 Thrane, J.-E., Kyle, M., Striebel, M., Haande, S., Grung, M., Rohrlack, T., and Andersen, T.: Spectrophotometric
1026 analysis of pigments: a critical assessment of a high-throughput method for analysis of algal pigment mixtures by
1027 spectral deconvolution, PloS one, 10, e0137645, 2015.
1028 Wang, G., Lee, Z., Mishra, D. R., and Ma, R.: Retrieving absorption coefficients of multiple phytoplankton
1029 pigments from hyperspectral remote sensing reflectance measured over cyanobacteria bloom waters, Limnol.
1030 Oceanogr., Meth., 14, 432-447, 2016.
1031 Wright, S. W., and Jeffrey, S. W.: Pigment markers for phytoplankton production, in: Marine organic matter:
1032 biomarkers, isotopes and DNA, The Handbook of Environmental Chemistry, edited by Volkman, J. K., Springer,
1033 Berlin, Heidelberg, Germany, 71-104, 2006.